UNIVERSITY *of* TASMANIA

The Temperature Distribution and Geothermal Heat Flux at Law Dome, East Antarctica

by

Syed Abdul Salam

B.Sc. Electrical Engineering
M.Sc. Electrical Engineering

Submitted in fulfilment of the requirements for the degree of
Master of Science (Natural and Physical Sciences)

Institute for Marine and Antarctic Studies (IMAS)
College of Sciences and Engineering
University of Tasmania

November 2020

Abstract

The East Antarctic Ice Sheet (EAIS) is the world's largest potential source of sea-level rise, with the marine-based component (i.e. where the ice sheet is grounded below sea level) containing enough ice to raise sea levels by 52 m. Ice dynamics are strongly influenced by the internal temperature distribution within the ice sheet, with warmer, more deformable ice leading to potential increases in ice-flow velocities, discharge of ice into the ocean and global sea-level fluctuations. Therefore, accurately quantifying englacial ice temperature has the potential to help refine projections of the Antarctic ice-sheet contribution to global sea-level change.

Direct temperature measurements through borehole drilling within the ice sheet are reliable but are very sparse over Antarctica. This is because it is very expensive, slow to acquire, and logistically challenging to obtain direct measurements of ice temperature. To mitigate this, one approach is radar-echo sounding, which is a powerful and widely used method to constrain temperatures on basin to continental-scales.

Law Dome is a small independent ice cap (approximately 200 km diameter) situated to the west of Totten Ice Shelf in East Antarctica. The region of Law Dome is an appropriate target for investigating englacial temperatures because of the good coverage of airborne radar data from the Investigating the Cryospheric Evolution of the Central Antarctic Plate (ICECAP) project and a temperature profile to bedrock from within an ice borehole at Dome Summit South (DSS). Also, this ice cap is slow-moving and stable with a low melt-rate (2.9 m/yr) at the surface due to the moderate wind speed (mean wind speed 8.3 m/sec), which makes it a good case study region.

Here, we use radar data to detect the englacial reflectors in the ice, followed by the estimation of the radar attenuation rate. Previous methods used either estimates of the depth averaged value of the attenuation rate or required additional information regarding the englacial reflectors (stratigraphy), which is not the case here. The extraction of the attenuation rate from radar data is mathematically modelled as a constraint regularised l_2 minimisation. Once the attenuation rate is estimated, these attenuations are mapped to temperature profiles. The attenuation is greatly affected by ice temperature and ice chemistry. It is assumed that the ice chemistry will remain the same over Law Dome and the ice borehole temperature profile at DSS is used for calibrating the attenuation-temperature mapping function. The gradient of these temperature profiles is used to obtain geothermal heat flux (GHF) using Fourier's heat flow equation.

To validate our methodology, attenuation differences at flight crossover points are calculated and statistical analyses performed to assess the accuracy of the results. Both spatial and depth analysis are performed over these crossovers. In spatial analysis the differences are averaged over the depth and in depth analysis it is averaged over the spatial dimension. For spatial analysis, the differences are of the order 22.6%, 15.2%, and 32.8% for mean absolute deviation, median absolute deviation, and root mean square error respectively. Also, for the depth analyses, up to the depth of 800 m, the errors are under 29.8%, 24.2%, and 38.8% for mean absolute deviation, median absolute deviation, and root mean square error respectively.

The products obtained are 3-D radar attenuation rate of the region, temperature profiles along the ice-column, basal temperature, and GHF across Law Dome. The resulted GHF values are in the range 65-80 mWm^{-2}. All data sets have high spatial resolution (1km x 1km grid) and are compared with the previously available GHF for the region.

A novel method is developed which shows how raw radar sounding data can be used to estimate the attenuation rates, temperatures, and GHF. This method utilises a special case of Ridge regression for estimation of high resolution data sets. In comparison to the existing GHF maps, this method has high resolution and it only requires raw radar data and a single temperature profile over several hundred kilometres.

Declaration of Originality

"This thesis contains no material which has been accepted for a degree or diploma by the University or any other institution, except by way of background information and duly acknowledged in the thesis, and to the best of my knowledge and belief no material previously published or written by another person except where due acknowledgement is made in the text of the thesis, nor does the thesis contain any material that infringes copyright."

Syed Abdul Salam

Nov 05, 2020

Statement of authority of access

The publisher of the paper comprising Chapter 2 hold the copyright for that content and access to the material should be sought from the respective journal. The remaining non published content of the thesis may be made available for loan and limited copying and communication in accordance with the Copyright Act 1968.

Syed Abdul Salam

Nov 05, 2020

Statement of Co-Authorship

The following people and institutions contributed to the publication of work undertaken as part of this thesis:

Candidate: Mr. Syed Abdul Salam, *IMAS, UTAS*

Author 1: Prof. Richard Coleman, *IMAS, UTAS*

Author 2: Dr. Jason L. Roberts, *AAD Australia*

Author 3: Dr. Felicity S. McCormack, *School of Earth, Atmosphere & Environment, Monash University*

Author 4: Dr. Jacqueline A. Halpin, *IMAS, UTAS*

Contribution of work by co-authors for each paper:

Paper 1: Located in Chapter 2

Abdul Salam, Syed, Roberts, J. L., McCormack, F. S., Coleman, R., and Halpin,J. A. A 3D map of englacial attenuation rate from radar reflections at Law Dome, East Antarctica. (under review for *Earth System Science Data*)
https://essd.copernicus.org/preprints/essd-2020-146

Author contributions: The candidate is the primary contributor and the other authors contributions are supervisory in nature. Author 1 contributes to the writing iterations and helped with the ideas of the method validation (crossover analysis). Author 2 contributed more on technical side of the paper which includes mathematical formulation and layer detection. Author 3 contributed in broader context of how the work fill the gap in ice-sheet modelling, generating the maps and writing iterations of the paper. Author 4 contributions are more towards the implications of the generated attenuation rates for englacial temperature geothermal heat flux.

Paper 2: Located in Chapter 3

This chapter is planned to be submitted soon to *Journal of Glaciology.*

Author contributions: This paper is still in progress but the main theme of the paper is already decided. The candidate is the primary contributor and the other

authors contributions are supervisory in nature. Author 1 assisted with the alternate mapping function to the Arrhenius mapping function. Author 2 helped with the advective correction mechanism of geothermal heat flux. Author 4 expertise helped in the interpretations of the englacial temperatures and geothermal heat flux.

We the undersigned agree with the above stated proportion of work undertaken for each of the above published (or submitted) peer-reviewed manuscripts contributing to this thesis:

Signed:

Syed Abdul Salam	**Prof. Richard Coleman**	**Prof. Neil J Holbrook**
Candidate	Primary Supervisor	Centre Head, Oceans and Cryosphere
Institute for Marine and Antarctic Studies	*Institute for Marine and Antarctic Studies*	*Institute for Marine and Antarctic Studies*
University of Tasmania	University of Tasmania	University of Tasmania
Date: Nov 05, 2020	10 November 2020	10 November 2020

Acknowledgements

I would like to thank and express my sincere gratitude to my primary supervisor, Prof. Richard Coleman, co-supervisors, Dr. Jason L. Roberts, Dr. Felicity S. McCormack, and Dr. Jacqueline A. Halpin. I thank my supervisory team for their support, motivation, and endless patience throughout my thesis. This dissertation would not have been possible without their guidance, constructive feedback, and encouragement.

I thank Institute for Marine and Antarctic Studies (IMAS), University of Tasmania for providing the platform to conduct my research. I also thank Antarctic Gateway Partnership (AGP) Scholarship for financial assistance which enabled me to do my research.

Last but not least, to my family members including my grandfather whom I lost during this thesis. I would like to express my gratitude for their unconditional love and support.

In memory of my father and grandfather.

Contents

List of Figures

Chapter 1

Introduction

> The IPCC Fifth Assessment Report (AR5) concluded that, 'Warming of the climate system is unequivocal, and since the 1950s, many of the observed changes are unprecedented over decades to millennia. The atmosphere and ocean have warmed, the amounts of snow and ice have diminished, sea level has risen, and the concentrations of greenhouse gases have increased' [2].

The Antarctic ice sheet is the world's largest potential contributor to sea level rise. It has been losing mass over past decades through the accelerated flow of its glaciers, conditioned by bed topography and warm ocean temperatures [3]. Antarctica has a sea level rise equivalent of 58 m (57.9 ± 0.9 m from Bedmachine [3]; 58.3 m from Bedmap2 [4]) and the East Antarctic region has the potential of approximately 52 m sea level rise. East Antarctica has lost 50 ± 13 Gt/yr ice from 2009-2017, 20% of the total Antarctic mass loss [3, 5].

Despite advancements in numerical ice sheet modeling in the estimation of sea level projections, there remain unknowns in key processes, model parameters, and boundary conditions that impact the uncertainty associated with projections of sea

level rise. For example, englacial temperatures and geothermal heat flux (GHF) are two poorly constrained parameters that can have a large impact on ice dynamics [6, 7]. Ice temperature has an impact on flow rates [8], and is, therefore, a key parameter in understanding and predicting change in ice dynamics and mass loss.

Ice flows by viscous creep and basal sliding, and each of these processes depend critically on englacial temperature [9]. The temperature within ice sheets is therefore critical information for accurate modelling of ice sheet flow. Within ice sheets, an understanding of the temperature distribution is important for knowing its intrinsic properties and other physical processes related to it. The deformation rate of ice strongly depends on temperatures [9] and rapid glacier sliding can occur when the basal temperature approaches the pressure melting point, producing subglacial melt water [9–12]. It is essential to characterize ice sheets' thermal regimes in order to constrain the current state and predict the future evolution of an ice sheet.

In the last two decades, the basal thermal regimes of ice caps, mountains glaciers and large ice-sheets have remained a subject of intensive research [13–15]. GHF is one of the major uncertainties in understanding the basal conditions of the Antarctic ice sheet [16]. Under the ice-sheets, the variability in geothermal heat flux distribution is due to the thickness of the lithosphere, crustal heat production and variations in bedrock structure [17–21]. Direct measurements of GHF and englacial temperatures near the base of the ice sheet requires direct access to the ice-sheet bed, and is therefore typically limited to ice borehole sites. The East Antarctic region only has a handful of ice core sites which limits the number of reliable basal temperatures and GHF estimates [22–25]. With our non-invasive method, regions that have radar data and a temperature profile within a few hundred kilometres radius, high spatial resolution temperature and GHF maps can be generated.

The aims of this thesis are: 1) to derive a radar-based method for calculating englacial temperature records over basin spatial scales; and 2) use englacial temperature records to constrain GHF estimates. For the first aim, these steps are followed: a) derive radar attenuation for internal layers; and b) convert attenuation in (a) to temperature. In order to achieve the second aim, a thermal model approximation is utilised to estimate GHF given the englacial temperature profile estimated in (b).

Direct measurements of englacial temperature generally requires borehole drilling, which is logistically challenging and time-consuming, and not feasible at basin to continental scales [26]. Direct measurements of englacial temperature (down to the bedrock) in the East Antarctic Ice Sheet (EAIS) are restricted to the ice boreholes at Dome Fuji [22], Dome South Summit (DSS) [23], Vostok [24], and Dome C [25]. As an alternative to borehole drilling, there are several geophysical methods for studying the ice sheets, including seismic surveys [27], magnetometry [28], gravimetry [29], satellite altimetry [30] and ice penetrating radar [26, 31–36]. These geophysical methods are used as indirect methods for measurements of englacial and subglacial properties including the thermal regime of the ice sheet [26, 31–39]. Among these indirect methods, seismic and ice penetrating radar methods have been used to infer englacial temperatures [26, 33, 37].

In seismic methods, the attenuation is used as a proxy to infer englacial temperatures from seismic reflections [37]. Seismic attenuation is sensitive to lithology, fluid content, porosity, and anisotropy [40, 41], but temperature is the most important control on seismic attenuation within the ice, particularly when the attenuating medium approaches its bulk melting point [37]. Peters et al. [37] presented a novel approach to constrain englacial temperature through an ice sheet by active seismic methods. The seismic quality factor Q (or internal friction) is calculated

to estimate the temperature profiles. With increasing depth, the value of Q is decreased, which suggests an increase in temperature.

Similar to seismic attenuation, radar attenuation within ice also depends on temperature, and this temperature dependence is arguably better constrained than the seismic attenuation [26, 33, 42]: radar surveys can be conducted both on ground and through aircraft while seismic is only ground based. The seismic surveys are slower than airborne radar surveys for the same area of coverage. However, seismic data provides offset reflections, which provides more information about the englacial layers. The radar data is available in abundance and have larger coverage areas than seismic data over Antarctica [3, 4].

The radar surveys conducted in the last five decades have transformed our understanding of glacier and ice sheet beds and how ice flows over them [43]. Radar sounding (or ice penetrating radar) is a powerful geophysical approach for characterising the subsurface conditions of ice masses [26, 31–36, 43]. Radar sounding has been used in glaciology to infer bed topography [3, 4, 44], ice thickness [3, 4, 44–46], and englacial layers [26, 47–49] of the ice sheets. A majority of ice penetrating radar surveys have been motivated by the primary objective of locating the bed reflectors. These bed reflectors are then used either to map the bed topography or to estimate the total volume of ice, which is needed to estimate the sea level rise potential of the ice sheets [4, 50–52]. In addition to resolving bed topography, the radar sounder equations can also be solved either for basal reflectivity or echo character to investigate the thermal, material, and geometric properties of the basal interface [32, 53–57], the distribution of subglacial water [53], englacial temperatures [26], the spatial variation of basal melt [46, 58], the transition between frozen and thawed bed conditions [38, 59, 60], and histories of surface accumulation [61].

The measured power of a reflected radar wave preserves information from bed reflector, englacial reflectors, and path effects (which includes all the path losses;

such as geometric, scattering, dielectric absorption which corresponds to attenuation, and birefringence etc.). Thus, the returning waveforms provide insight into the nature of subsurface interfaces and the ice column [62]. In polar ice sheets, attenuation is generally the strongest path effect [63]. The returned power from an ice-bed interface is normally corrected for the attenuation losses, either through empirical [39, 64, 65] or numerical methods [60, 66]. After attenuation and other power loss corrections (discussed in chapter 2), the returned power from the bed can be interpreted in terms of bed properties; such as wetness ([32, 67] and roughness [67–69]). Both wetness and roughness affect glacier processes like basal slip [70, 71]. Recently, attenuation rates have also been used to infer the ice column properties such as ice temperature [26] and water content in the firn [72].

Laboratory analyses and field data suggests that relatively homogeneous ice is a very low-loss medium (resulting in a relatively small loss of returned power englacially due to dielectric absorption) for radio waves at VHF (30– 300 MHz) frequencies [43]. Dielectric absorption of ice is proportional to its electrical conductivity, which is related to the ice temperature and chemical properties of ice [42, 73–76]. As dielectric absorption is strongly dependent on temperature, variations in the attenuation rate can be used to estimate englacial temperature. The electrical conductivity of pure ice (both *in situ* and laboratory-grown) is approximately 0.01 mSm^{-1} [73]. However, the electrical conductivity is also influenced by chemical impurities in the ice [34, 48, 66]. Assuming constant impurity concentrations over length scales of several hundred kilometres. This assumption will enable us to use a single temperature profile for attenuation-temperature mapping over Law Dome which is approximately 200 km in diameter [23].

There are a number of empirical and modelling methods to derive attenuation. Empirically, many methods use bed echoes to constrain the attenuation, ranging from a simple linear fitting model to adaptive constraining attenuation or model

informed fitting [39, 59, 64, 65, 77]. Englacial layer information can also be used to derive attenuation rates [26, 48]. Besides empirical methods, attenuation can also be modelled and can be compared to observations to constrain the englacial temperatures [66]. Prior studies used either paired conductivity and thermodynamic models or radar data directly to calculate attenuation, but there is not a single standard method available so far [62]. Hills et al. [62] argued that for the same input radar data if different attenuation methods are applied, it yields varied results.

Broadly, the attenuation methods can be divided into three groups: a) inferring attenuation from a single reflector across many traces [38, 39, 64, 78–80]; b) inferring attenuation from multiple reflectors within one trace [26, 48]; and c) inferring attenuation by contrasting the measured power from primary and secondary reflections [67, 81]. Methods that rely on a single reflector calculate a single attenuation value over the ice-column. However, this does not yield information on the englacial temperature profiles with depth. For methods which infer attenuation from multiple reflectors, there are two options, i.e., depth-averaged and depth-resolved. The depth-averaged method again results in a single value attenuation rate while the depth-resolved provides enough information to estimate the temperature profile over the ice-column [26, 48].

Law Dome is selected as a case study region for estimating its attenuation rates, englacial temperatures, and geothermal heat flux. Law Dome ($66.7°S, 112.8°E$) is a small independent ice cap (2.2 ± 0.1 cm sea level rise equivalent [3]) on the Budd Coast of Wilkes Land, about 125 km ESE of Casey Station, East Antarctica. Law Dome has been the subject of a number of glaciological and geophysical surveys since 1962 [82]. Fig. 1.1 shows the location of Law Dome in East Antarctica and the blue rectangle in the figure shows the selected region for this thesis. Investigating the Cryospheric Evolution of the Central Antarctic Plate (ICECAP)

[83, 84] project is an aerogeophysical survey over East Antarctica which provides a dense radar data over the region. ICECAP radar data is our main input data for extracting attenuation rates. For mapping these attenuation rates to temperature profiles the ice core temperature profile at Dome Summit South (DSS) is utilised which is an approximately 1200 m deep surface-to-bedrock drilling site [23, 85]. The ice on Law Dome is stable and slow-moving, and there is negligible melting at the ice surface [86] and relatively moderate wind speed (8.3 ms^{-1}) [87], which means that the englacial layers are relatively stable.

The overarching aim here is to extract englacial temperatures from radar data. The first step is to develop a method to obtain the radar attenuation from radar reflections as outlined in Chapter 2 (*Chapter 2 is submitted to Earth System Science Data (ESSD)*). In this process the englacial reflectors are detected automatically and a regularised mathematical model is developed to estimate the attenuation rates. In the second stage, these englacial attenuation rates are transformed into englacial temperatures as outlined in Chapter 3 (*Chapter 3 is planned to be submitted to the Journal of Glaciology*). This transformation requires the assumption that the chemical properties will remain the same throughout the region of Law Dome as a single temperature profile [23] is used to obtain the mapping function. This mapping function simply transforms the attenuation rates to englacial temperatures. Once the temperature profiles are obtained the gradient of these temperatures are then used to estimate the distribution of GHF across Law Dome [91–93]. This requires several assumptions including that there is no horizontal advection and no additional heating source from basal shear. The thermal gradient can also be affected by factors other than GHF like surface temperature; however, we considered the estimated temperature near the ice sheet bed which reduces the influence of the surface temperature. The estimated GHF values are slightly lower than the previously estimated value of 72 mWm^{-2} [23] at DSS. However,

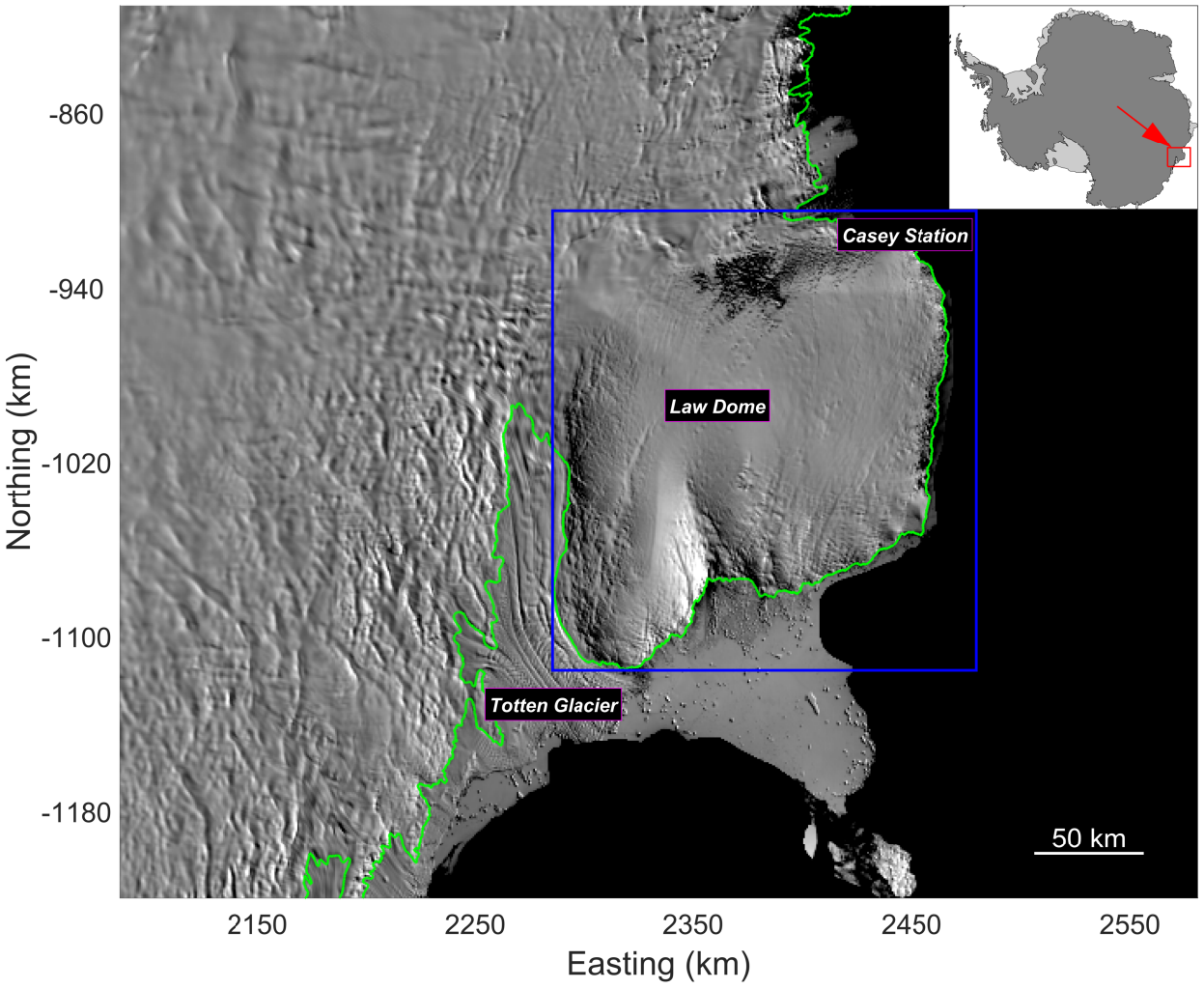

FIGURE 1.1: Our area of interest (Law Dome) is enclosed in the blue rectangle and the green line shows the grounding line. The background image is from Moderate Resolution Imaging Spectroradiometer (MODIS) over Antarctica for the 2008-2009 austral summer season [88, 89]. The figure is generated using Antarctic Mapping Tools for MATLAB [90].

our estimates are not exactly at the bed, and much of this difference is removed when a correction for vertical advection is applied. This correction is applied to obtain the final GHF at DSS.

In this thesis, a new method is developed for attenuation rates. This method is important because it requires radar data and there is no need for details of englacial layers or any other details about reflectivity within the ice. It automatically detects

the reflectors in the ice column. Our method provides a 3D volume of attenuation rates which is helpful for generating temperature profiles along the ice column over Law Dome. In addition to using attenuation as a proxy for temperature profiles, it can also be used to correct the power reflected from englacial layers and the bed. This will improve the radar reflections and its interpretation will lead to even better understanding of subglacial environments. This method can easily be extended to other regions having radar data and temperature profiles.

Chapter 2

Attenuation rates

2.1 Introduction

The East Antarctic Ice Sheet (EAIS) is the world's largest source of sea-level rise, with the marine-based component (where the ice-sheet is grounded below sea level) containing enough ice to raise sea levels by approximately 52 m [3, 5]. The rate of the potential EAIS contribution to sea-level rise can be estimated by calculating the ice-sheet mass budget. Ice dynamics play an important role in the ice-sheet mass budget by transporting ice from areas of accumulation to areas of mass loss. Ice transport is strongly influenced by the internal temperature distribution within the ice-sheet, with warmer, more deformable ice leading to potential increases in ice-flow velocities [94, 95], greater discharge of ice into the ocean, and global sea-level fluctuations. Estimating attenuation rates and temperatures from ice penetrating radar has the benefit of constraining important model parameters (e.g. GHF in the thermal model) that can be used in simulations of present-day ice dynamics, as well as simulations of the EAIS contribution to future sea level rise.

Radar-echo sounding (RES) is a powerful and widely used geophysical method to characterise the physical properties of the ice medium, such as ice thickness, temperature, and englacial structure of ice-sheets and glaciers [26, 31–36, 96]. The basis for RES is the detection of transmitted electromagnetic waves reflected from within the ice-sheet; the attenuation, transmission and reflection of these waves is controlled by the electrical conductivity and permittivity of the ice [97]. As conductivity and permittivity are functions of the ice chemistry, they vary spatially and through the ice column (or englacially), impacting the strength of the reflectivity, and enabling the exploration of the physical properties of englacial ice structures [32, 39]. The attenuation rate is primarily controlled by the ice-sheet's temperature and chemistry [34, 66, 98], and can be used to characterise the physical properties of ice.

Previously, many studies assumed englacial attenuation rates to be uniform within the ice and proportional to the ice thickness [99–101]. However, the attenuation rate varies with location, due to changes in ice properties [34, 63]. For example, a study in central West Antarctica shows that the one-way depth-averaged attenuation rate varies horizontally by 5 $dB\ km^{-1}$ in absolute terms along radar transects [98]. Matsuoka et al. [63] argued that the assumption of regionally uniform attenuation rate fails in most cases due to varying ice chemistry and temperature which leads to false attenuation estimates. However, these studies explored attenuation rates only in small regions and the understanding across broader spatial scales needs to be improved.

MacGregor et al. [26] demonstrated the use of radar reflections from englacial layers to constrain the attenuation rates and temperatures as a function of depth in the Greenland ice-sheet. A key advantage of the method derived by MacGregor et al. [26] is that it does not rely on echoes from the ice-sheet bed to determine attenuation, as the bed is complex and spatially variable [79], complicating interpretation

of radar data near the bed. The disadvantage of this method is that it requires radiostratigraphy (study of layering by means of radar reflections) data to reliably trace the englacial layers [26]. Many studies considered inferring the englacial attenuation or temperature from airborne radar data [26, 34, 39, 102, 103], but none have done it in a way that only relied on radar data.

Another radar-based method to constrain attenuation rates was proposed by MacGregor et al. [33]. In this method, it assumed constant reflectivity values for the internal layers and the method also exploits the dependence of radar attenuation on ice temperature. However, this approach requires undisturbed englacial layers (i.e., having clear boundaries in englacial layers), which cannot be applied to many important regions because of the lack of englacial layer information. This depth-averaged method is applicable at the ice-sheet scale, which requires contiguous and undisturbed englacial layers, and cannot be applied to areas which include highly-crevassed and fast-flowing regions near grounding zones and shear margins [26]. However, as these regions often influence the dynamics of the ice-sheet to a greater extent, layer-based approaches cannot be used to obtain englacial temperatures in many critical areas for ice-sheet modelling.

As an alternative to the methods described above, Schroeder et al. [39] developed an adaptive approach for estimating englacial attenuation rates for the entire ice column in Thwaites Glacier, West Antarctica. In this method, the unfocused radar bed echoes are fitted based on the correlation of ice thickness and the corrected bed power echo. The method performs weakly across the catchment near steeply sloping bed topography. In addition, another concern is that this method returns a 2D spatial map; however, deriving englacial temperatures requires estimates of attenuation throughout the ice column, requiring a 3D attenuation map. The temperature gradient can then be used to constrain the geothermal heat flux in the ice-sheet.

Our proposed method overcomes some of the limitations of the previous methods. Initially, the englacial reflectors are detected in the reflection data and then a mathematical technique that minimises the mismatch is used to obtain the estimates of englacial attenuation. This method does not require any additional datasets (such as englacial stratigraphy). Therefore, this method can be applied to regions which only have radar-bed echoes. A large amount of radar data has already been acquired for a number of purposes across vast areas of the ice-sheet. This method can utilise the existing acquired data and will extract the attenuation rates, which can further be used to estimate temperature profiles; consequently, it can improve the geothermal heat flux maps and ultimately can help improve ice-sheet modelling predictions. The 3D map of englacial attenuation rate is not available from any previous study and it can be a good data set for testing different novel algorithms. Here, the radar data from the Investigating the Cryospheric Evolution of the Central Antarctic Plate (ICECAP) [84] mission for Law Dome East Antarctica are used. In the next section, the importance of the Law Dome region is discussed. Section 3 describes the methodology used for estimating the englacial attenuation rates. An assessment of the quality of the results, crossover and uncertainty analyses are presented in Section 4. A summary of the research findings is presented in section 5, including the derived 3D map of attenuation rates and their uncertainty.

2.2 Study region and input data

Law Dome $(66.7°S, 112.8°E)$ is a small independent ice cap (approximately 200 km in diameter) which is situated on the coast of East Antarctica as shown in Fig. 2.1. Law Dome is a suitable case study for estimating attenuation for a number of reasons: 1) the availability of well-sampled radar data from the ICECAP [84]

project, an aerogeophysical survey over East Antarctica; 2) the ice core drilling site of an approximately 1200 m deep surface-to-bedrock at Dome Summit South (DSS) which is located approximately 4.7 km SSW of the Law Dome Summit at an elevation of 1370 m [23, 85] which can be helpful in mapping attenuation to temperature profiles; and 3) the ice on Law Dome is slow-moving and stable, and there is negligible melting at the ice surface [86] and relatively moderate wind speed (8.3 ms^{-1}) [87], which means that the englacial layers are relatively stable.

The ICECAP geophysical data that we use in this study were collected over the period 2008-2012, covering over 14800 line-km of the Law Dome region [83, 84]. The survey aircraft was fitted with a High Capability Radar Sounder (HiCARS) instrument, with a central frequency of 60 MHz and bandwidth of 15 MHz. In order to retain full energy of the radar reflections, the radar data was processed after pulse compression [104]. Ice thickness was determined using an ice speed of 169 $m/\mu s$ for electromagnetic wave propagation and no firn correction was applied for the reduced velocity of radio-waves [84]. In this work the bed-echo and aircraft height data will be used in order to extract the attenuation rate. The selected data cover the entire Law Dome region as shown in Fig. 2.1.

The spatial resolution of the ICECAP radar data is approximately 20 m along the flight lines while the spacing between the flight lines is in order of kilometres and is not evenly sampled (see Fig. 2.1).

2.3 Methodology

We use radar reflectors from within the ice column to estimate radar attenuation. Radar attenuation is the loss (dB) of signal strength due to dielectric absorption [106, 107], scattering and geometrical spreading. The attenuation rate given by following Equation 2.1 describes the loss of energy from source to receiver per unit

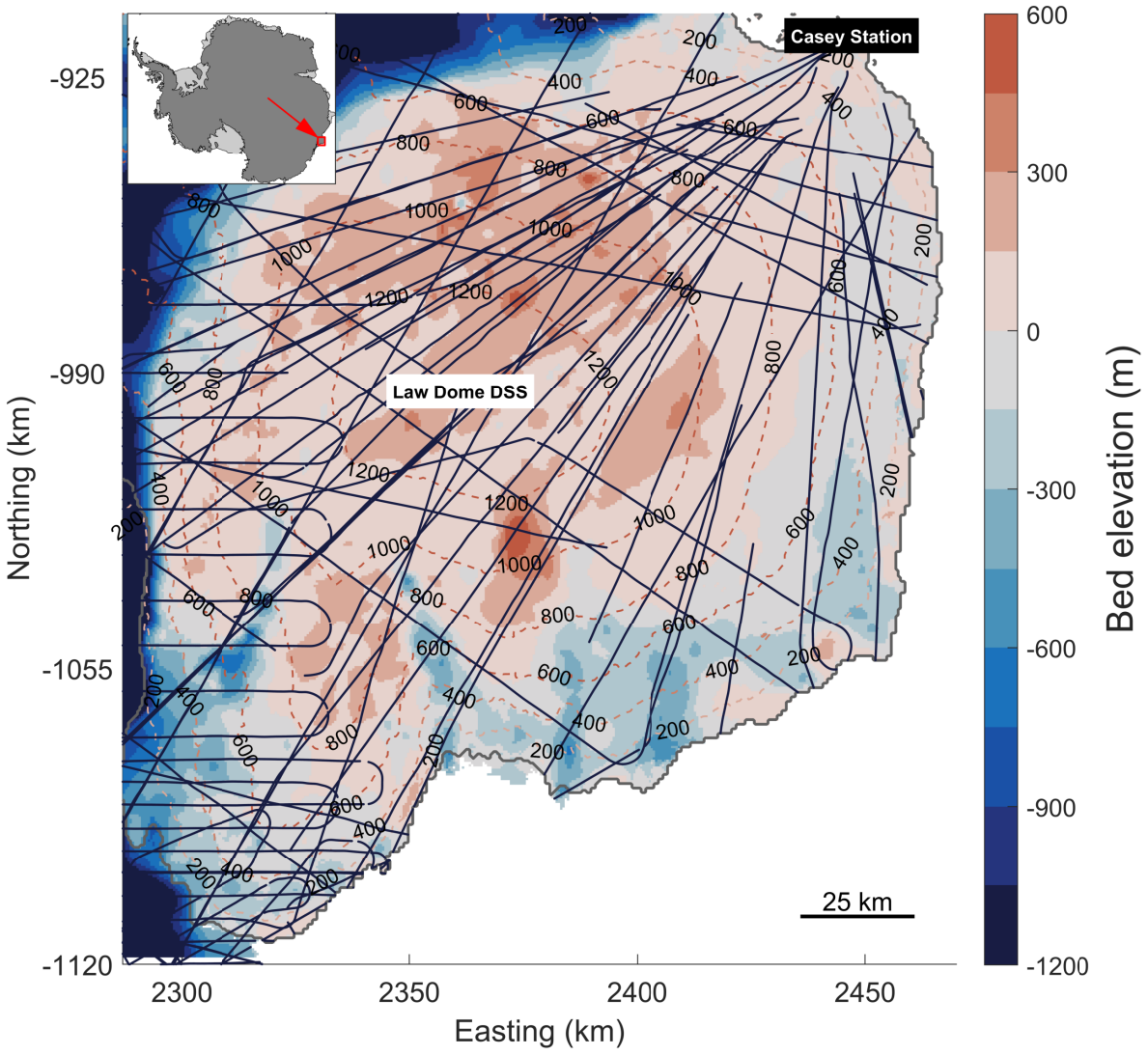

FIGURE 2.1: The black lines show the radar coverage over Law Dome from ICECAP project [83, 84, 105]. Data from 2009-2012 is shown. The bed elevation (shading) and surface elevations (contours) are from BedMachine Antarctica. The projection is polar stereographic (true latitude 71S) and the bed and surface are relative to EIGEN-EC4 geoid [3, 90].

distance [97].

$$N = \omega \left\{ \frac{\epsilon}{2} \left[\left(1 + \frac{\sigma}{\omega^2 \epsilon^2} \right)^{1/2} - 1 \right] \right\}^{1/2} \tag{2.1}$$

The attenuation rate (N) strongly depends on electrical conductivity (σ) , permittivity (ϵ) and angular frequency (ω). As some of these properties are themselves strongly dependent on temperature, variations in the attenuation coefficient can

be used to estimate englacial temperature, subject to making assumptions, such as constant conductivity (same chemical properties). Radar attenuation is proportional to conductivity and depends on the ice chemistry/acidity, but it varies slowly spatially. In the case of Law Dome, the concentrations of impurities in the ice column are low [86].

In our analysis of radar reflectors from within the ice column, the first crucial step is to locate the englacial layers with an assumption of having the same reflection strength, and all the reflectors are assumed to be specular (mirror-like) [35]. Once the englacial layers are detected down the ice column, the located depth and strength of radar can be used to infer the attenuation rate. The resulting attenuation rate can be validated by using crossovers of the flight lines to check the robustness of the method and estimate the uncertainty in the obtained attenuation.

2.3.1 Locating reflectors

In locating the reflectors, we process each vertical ice column of radar data (also known as a trace) independently to produce high resolution spatial data at approximately every 20 m. For a column with M reflectors ($M-1$ englacial layers), where the index i shows the i^{th} reflector from the surface, i.e., $i=0$ corresponds to the ice surface and $i=M-1$ corresponds to the lowest englacial reflector, the general equation for specular internal reflections from the i^{th} reflector is given by [26, 108]:

$$P_r^i = \frac{P_t(\frac{\lambda_{air}}{4\pi})^2 G_a^2 T^2 (L_a^i)^2 L_{vs} L_b L_{sys} G_p R}{4(h + d/\sqrt{\epsilon})^2}. \tag{2.2}$$

Here, P_t is the transmitted power, λ_{air} is the radar signal wavelength in air, G_a is the antenna gain, T is the transmission loss at the interface of air and ice, L_a is the one-way attenuation loss, L_{vs} is the total loss due to volume scattering, L_b is the loss due to birefringence, L_{sys} is the total system loss, G_p is the processing gain, h is the aircraft height above the ice surface, d is depth of the ice and ϵ is real permittivity of the ice. In the above equation, $P_t, \lambda_{air}, G_a, T, L_{sys}, G_p, \epsilon$ are assumed invariant for any given trace of radar data, which remains the same vertically down the trace, but can vary horizontally along the flight line. Similar to Matsuoka et al. [98], we assume that L_{vs} and L_b are negligible. The received signal power P_r^i from each reflector needs to be corrected first for the geometrical spreading so that the attenuation due to spreading of radiowave travelling down the ice column is compensated and the main attenuation factor should be only dependent on the ice properties. In Equation 2.3, the received raw radar signal is added with the geometrical correction factor (h distance travelled in the air and d within the ice), and then converted to decibels ($[x]_{dB} = 10log_{10}x$) for easier calculations. The radar sounding geometrically-corrected power is given by [26, 39]:

$$[P_g^i]_{dB} = [P_r^i]_{dB} + 2[2(h + d/\sqrt{\epsilon})]_{dB}, \tag{2.3}$$

where $[P_r^i]_{dB}$ is the received power in decibels.

After the power correction, the next step is to locate the englacial reflectors. Englacial layers have unique electrical properties, realised as peaks in englacial reflectivity. Sometimes there are false reflectors which means that two consecutive peaks may occur very close together, implying that the englacial layers are very thin. To avoid this situation, an assumption is made that englacial layers are no thinner than 60 m. These potential false reflectors make the process unstable and sometimes result in too many reflectors if the condition of minimum layer thickness is ignored. A value of 60 m was chosen as the minimum allowed spacing between

reflectors which is only at the detection stage of englacial layers. It means that no englacial layers detected can be closer than 60 m. Englacial layers can be spaced more than 60 m, this means our method can capture a vertical resolution of 60 m. The value of 60 m is the smallest value which gave an appropriate stable solution. Although for some regions around Law Dome, values less than 60 m also worked, for other regions it failed. This final selection was to make sure our method is stable for the entire region with the same layer value. In an example profile in Fig. 2.2, the detected reflectors are shown by small red circles. It can be seen that out of 14 reflectors, three reflectors are discarded because the attenuation rate is always positive and the signal is always attenuating over the depth. In other words, for constant strength reflectors, the resulting reflections will always lead to decreasing strength. However, the deeper layers can have higher reflectivity if they contain higher conductivity materials. The assumption of uniform layer reflectivity is a simplistic approach that we adopt at this current stage due to a lack of conductivity profiles at Law Dome. It will be worthwhile in the future to look into other approaches if englacial reflectivity data become available.

2.3.2 Retrieval of Attenuation

After detecting the englacial layers, the thicknesses of each englacial layer are calculated. Now, the attenuation rate estimation problem is formulated as a Ridge regularised minimisation problem [109]. In this problem, the required components are englacial layer thicknesses and strength of power from reflectors, while the attenuation rates are calculated. A penalty term is added to the minimisation problem to suppress unphysical high frequency oscillations due to overfitting but which provides a biased solution not relying 100 % on the data. The bias is controlled with the parameter λ, which controls the smoothness of the resulting attenuation. In other words, λ is controlling prior knowledge to the minimisation

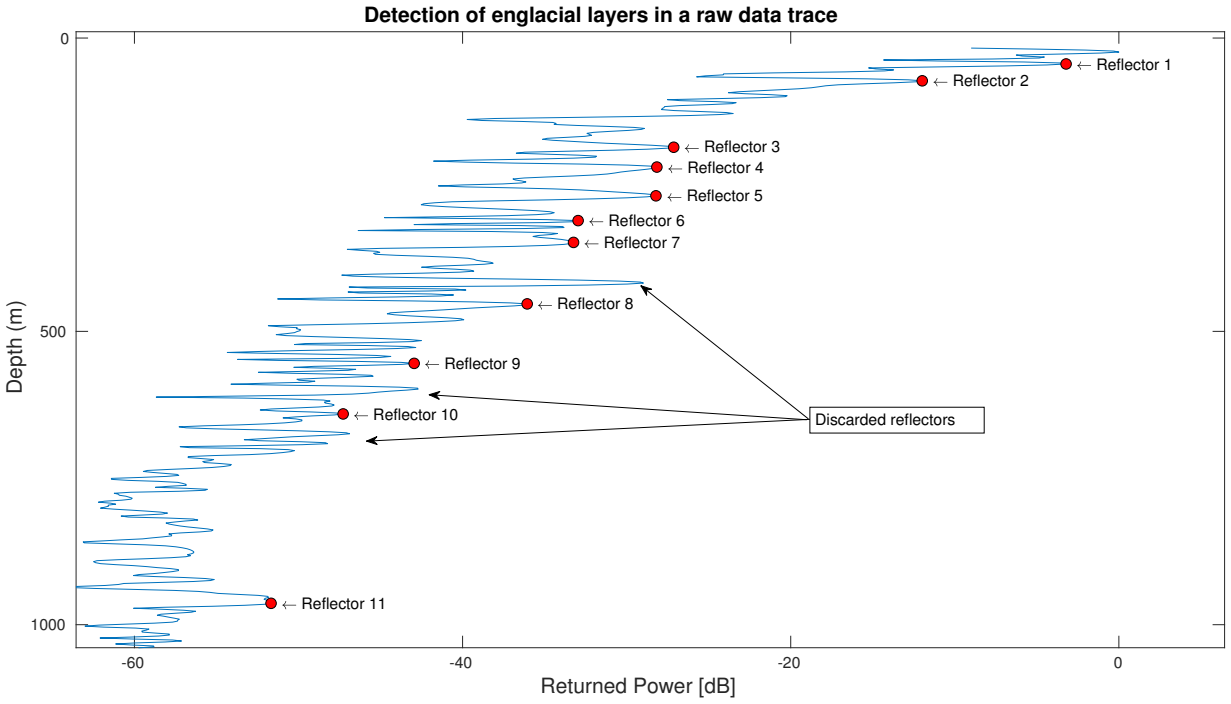

FIGURE 2.2: Locating englacial reflectors from a typical radar trace. The total detected reflectors here are 14 but three are discarded which leaves 11 englacial reflectors for further processing.

algorithm: the smaller the value, the more dependent the model is on the data and vice versa. When $\lambda = 0$, the problem becomes a minimisation of the least squares solution which means relying entirely on the data, but the solution may contain physically unrealistic oscillations. The given minimisation problem is as follows:

$$\min \left(\|Z * N - P\| + \lambda \|N\| \right) \tag{2.4}$$

$$subject \ \ to \ \ N \geq 0 \ ,$$

$$N = \begin{bmatrix} N_1 \\ N_2 \\ . \\ . \\ . \\ N_{M-1} \end{bmatrix}, \qquad P = \begin{bmatrix} P_1 \\ P_2 \\ . \\ . \\ . \\ P_{M-1} \end{bmatrix},$$

$$\mathbf{Z} = \begin{bmatrix} 1/\Delta z_1 & 0 & 0 & . & . & . & 0 & 0 \\ -1/\Delta z_2 & 1/\Delta z_2 & 0 & . & . & . & 0 & 0 \\ 0 & -1/\Delta z_3 & 1/\Delta z_3 & . & . & . & 0 & 0 \\ . & . & . & . & . & . & . & . \\ . & . & . & . & . & . & . & . \\ . & . & . & . & . & . & . & . \\ 0 & 0 & 0 & . & . & . & -1/\Delta z_{M-1} & 1/\Delta z_{M-1} \end{bmatrix}^{-1}$$

$$= \begin{bmatrix} \Delta z_1 & 0 & 0 & . & . & . & 0 & 0 \\ \Delta z_1 & \Delta z_2 & 0 & . & . & . & 0 & 0 \\ \Delta z_1 & \Delta z_2 & \Delta z_3 & . & . & . & 0 & 0 \\ . & . & . & . & . & . & . & . \\ . & . & . & . & . & . & . & . \\ . & . & . & . & . & . & . & . \\ \Delta z_1 & \Delta z_2 & \Delta z_3 & . & . & . & \Delta z_{M-2} & \Delta z_{M-1} \end{bmatrix},$$

where Z is the englacial layer thickness square matrix ($M-1$ x $M-1$), which contains the information of the thicknesses of all the englacial layers, Δz_i is thickness of i^{th} englacial layer, N is the radar signal two-way attenuation rate vector ($M-1$ x 1) within englacial layers, P is the power differences (in dBs) vector

$(M-1 \text{ x } 1)$ of the strongest reflection with each i^{th} layer and λ is the regularisation parameter to tune the model. Here, Z resulted in a matrix because we formulated for englacial layers attenuation (i.e. exactly within the layer) rather than total attenuation rate [26]. As we are assuming the englacial layers have the same strength reflections, which is not the case in reality, this may result in negative attenuation values. Negative attenuation is not possible so we enforce a constraint on the minimisation technique such that the resulting attenuation must be a non-negative value. Our formulated problem is not a simple Ridge regression, it has additional constraint of $N > 0$ which will not behave exactly simple Ridge regression, but the general behaviour is of Ridge regression.

In Ridge regression [110], selection of λ is main parameter. A higher value of λ will force the solution to be smoother but at the cost of diminishing the effect of data on the modelled solution. In addition, higher values of λ will also suppress attenuation towards zero (not exactly zero like lasso regression [111]). With higher value of λ, the optimisation cost function rely more on $\lambda \|N\|$ than the traditional least square error component. Our aim here is to find a value of λ which leads to a more robust and balanced solution. We explored number of values for λ ranging from $\lambda = 0$ to $\lambda = 10$. When the value exceeds $\lambda = 0.85$, the solution is physically unrealistic (extremely small values for the attenuation rate N), so $\lambda = 0.85$ becomes our upper bound. For lower values of $\lambda < 0.1$, the solution is too fluctuating (which are physically unrealistic and have large gradients) and for $\lambda > 0.85$, the resultant is unrealistically small values which in fact discard the role of the original data.

To find the optimum value of λ, mean square error (MSE) is plotted against λ as shown in Fig. 2.3, which shows the optimum range is approximately $0.3 \leq \lambda \leq 0.4$. When λ is in this range, the values of MSE are approximately close and we selected the smaller value because of two reasons. Firstly, the selected value of $\lambda = 0.3$

is on the lower side of the optimum range, resulting in adequate weighting of the original data, while avoiding large oscillations. Secondly, the normalised crossover differences are also lower for $\lambda = 0.3$ which is discussed in section 2.4.2.

Schroeder et al. [39] reported 0-20 $dbkm^{-1}$ one-way (or 0-40 $dbkm^{-1}$ two-way) attenuation rates at Thwaites Glacier, which is using a similar survey system of ours (HiCARS with frequencies ranging from 52.5 Mhz to 67.5 MHz). The reported value of attenuation rates helped us to determine acceptable range of attenuation rates for a similar system. Attenuation rates varies with frequencies and survey systems, so it is important to consider radar survey system when comparing typical values of attenuation rates. The reported attenuation rates for the same system at Thwaites Glacier [39] helps us in determining a physically realistic attenuation rates at Law Dome. As we change the value of λ, the value of attenuation rate is also affected, because the amount of bias in solution depends on λ in Ridge regression. The higher the value of λ, the values of attenuation rates are pushed more towards zero. So, the reported attenuation rate in Schroeder et al. [39] helped us to constrain λ, which leads to acceptable physically realistic range of attenuation rates.

The primary disadvantage of this method is that numerous englacial layers must be correctly detected to reliably constrain the attenuation rate. Furthermore, in order to avoid dependence on false reflectors, several conditions are required to be met for processing the ice column, i.e., the ice thickness must be at least 200 m in depth and the number of internal reflectors must be greater than or equal to four.

2.4 Data quality

In this section, the compilation of 3D attenuation data from the processed traces is discussed in detail. As each trace is processed independently, the resultant

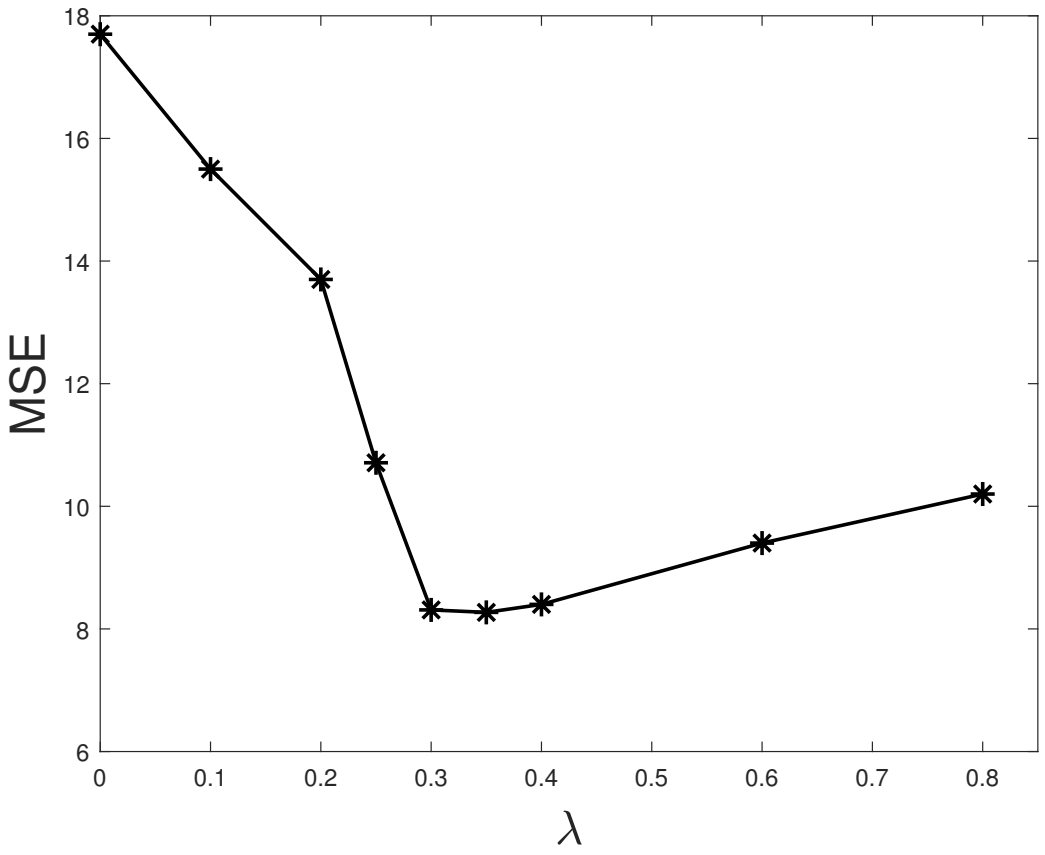

FIGURE 2.3: Mean square error (MSE) against λ to find the optimum values of λ. It can be seen that the MSE drops substantially at $\lambda = 0.3$.

attenuation rates are not well-distributed spatially over Law Dome. The reasons for this are: firstly, the flights do not follow uniformly spaced gridded paths; and secondly, the proposed method sometimes discards the traces with less than four internal reflectors or the ice thickness at that location is less than 200 m. For this reason, a 3D grid is generated which can help in visualising and binning the attenuation rates to the corresponding 3D cell.

Next, the results are further processed to calculate 3D distribution of the attenuation rates. In the 3D distribution, the 2D spatial coverage is 1 km x 1 km bins while each bin point is a trace down the ice column depth, at a spacing of 60 m. Each 3D cell point may be influenced by many independently processed radar traces. Many radar trace values may fall within a 1 km x 1 km bin, be a single

value in a bin or have no radar data. If there are many values falling in that 3D cell, the median is selected. The median values are selected for filling the grid because it performs better due to the reduced number and magnitude of outliers in the data. If no points fall within that cell, it will result in missing values (given as NaNs).

2.4.1 Depth-averaged attenuation and uncertainties

In this section, the processed data is visualised in terms of depth-averaged attenuation rate along with the uncertainties and the number of points spatially contributing to the plot. In the 3D grid, the spatial map over Law Dome is obtained by weighted average over all the depths in the traces. In the post processing of the attenuation results the following steps are done:

1. A 3D grid is created where each cell represents 1 km x 1 km x 60 m.
2. For each flight line, each trace is mapped to the closest cell in the 3D grid. We also have an additional 3D grid which retains information about how many values are contributing to the corresponding cell. Another spatial 2D version is added which represents how many traces from the flight lines are contributing to each bin (see Fig. 2.5).
3. The depth-averaged attenuation rate is calculated (see Fig. 2.4a).
4. Standard deviation within each bin is calculated in order to find the uncertainty in results (see Fig. 2.4b).

Fig. 2.4a shows the estimated englacial attenuation rate and the corresponding standard deviation in each bin is shown in Fig. 2.4b. As the flight spacing is non-uniform, there are different numbers of points contributing spatially, as indicated

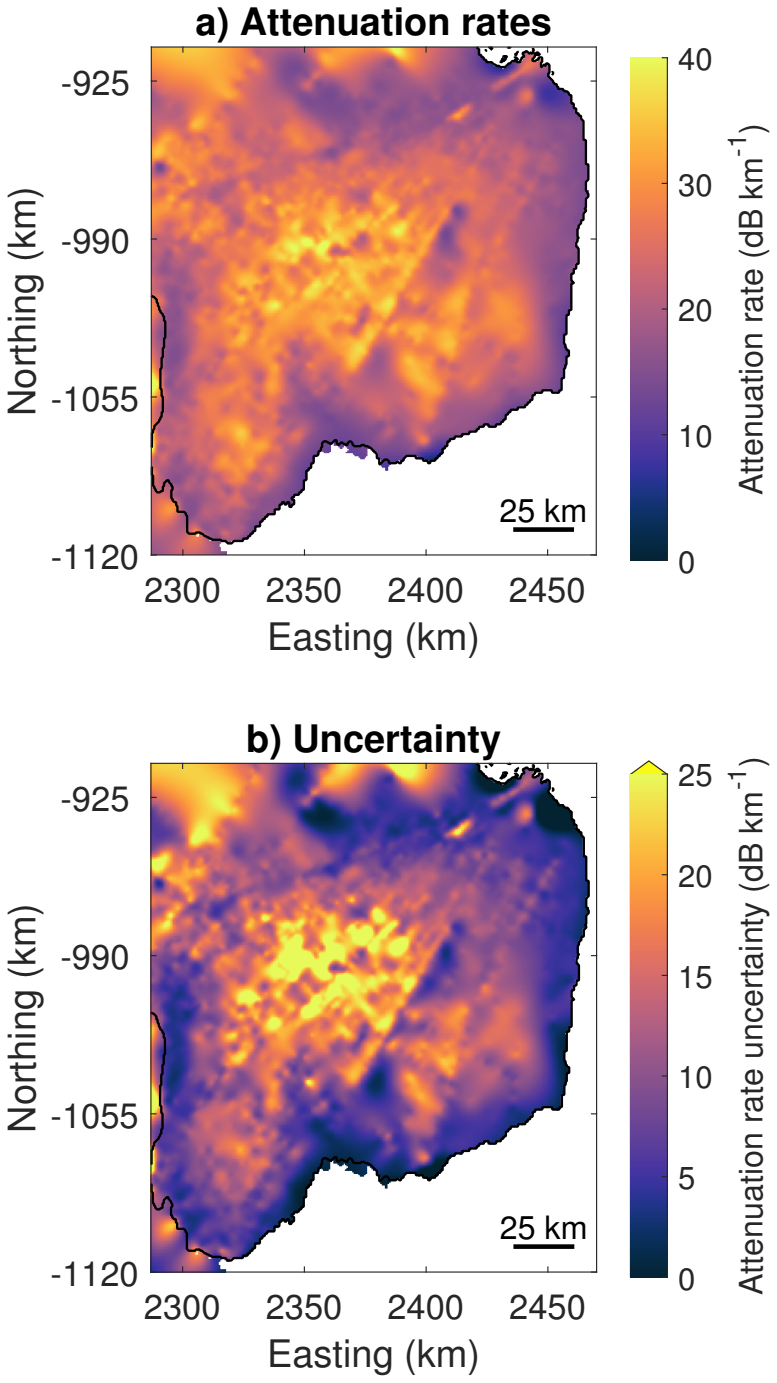

FIGURE 2.4: a) Spatially interpolated depth averaged attenuation rate. b) Standard deviation within the 1 km x 1 km bins of the depth averaged attenuation. The values of standard deviation are relatively small as compared to the absolute attenuation rate values which means the uncertainty in the processed attenuation rates are low. Note that the uncertainty increases at location with large thickness as the deeper reflectors are harder to detect correctly.

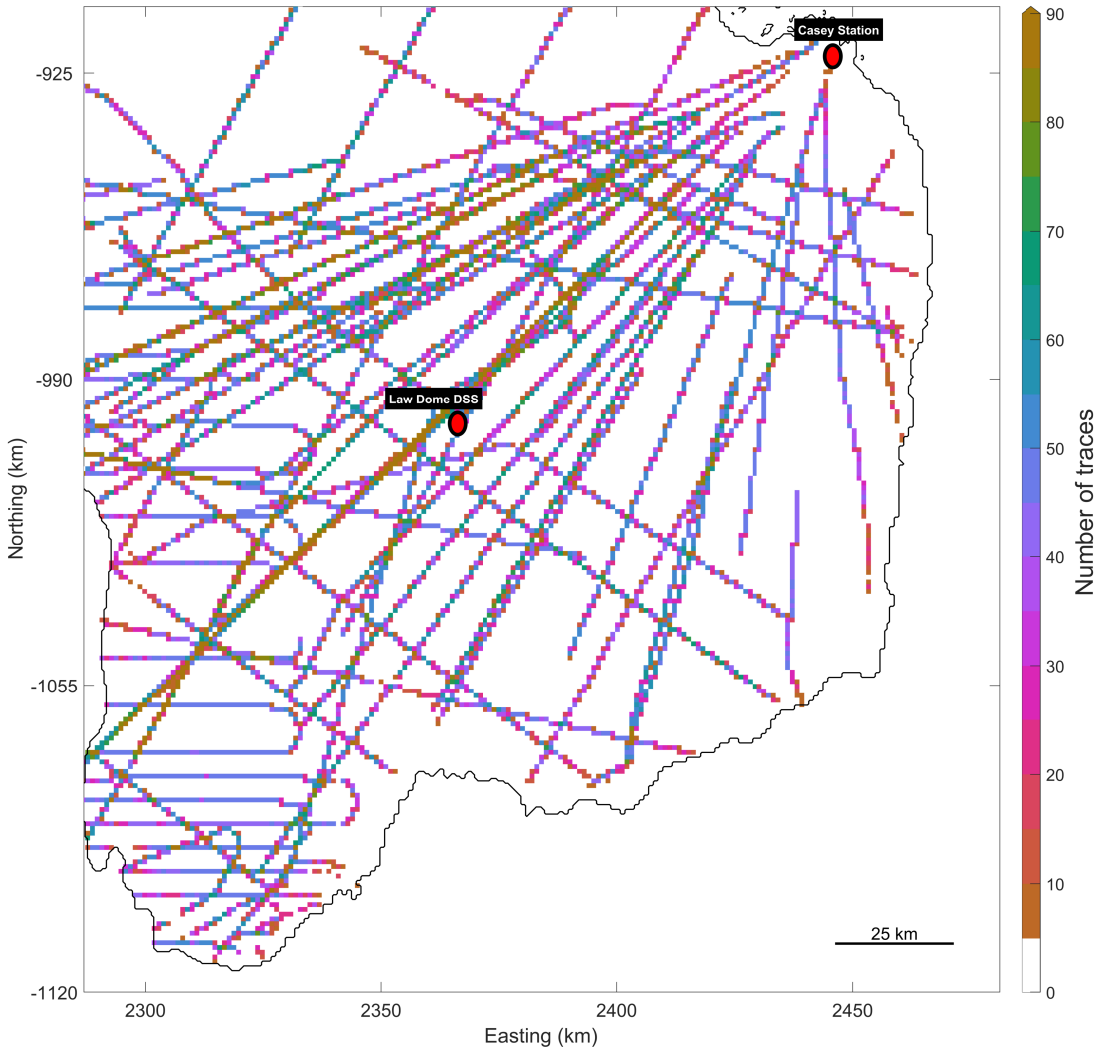

FIGURE 2.5: Number of traces contributing to each bin of the depth-averaged attenuation.

in Fig. 2.5. There are several linear artefacts in the attenuation maps. These artefacts are due to the geometry of the acquired flight tracks - the airborne flights were not acquired on a regular, equally spaced grid. Along the flight tracks, the spacing is approximately 20 m while the spacing between the flight tracks is of the order 30-40 km. Our method is applied trace by trace in each flight track, where a trace is a single column radar reflection. We later interpolated our final maps on a regular grid of 1 km x 1 km, but because of irregular geometry the final maps

have these artefacts. These artefacts can be minimised by applying a smoothing filter, but it will diminish our aim of high-resolution maps. Fig. 2.5 shows how many points are contributing to these grid cells, it is clear in the figure that the irregular distribution of the data points leads to these artefacts.

2.4.2 Crossover Analysis

In this section, the attenuation rate results are analysed at the crossover points in order to see the robustness of the method. A crossover is a location where two or more flight lines cross each other (here crossover is considered within 35 m). There are 582 crossovers. Here, we consider results averaged both over the depth and spatially.

In the first spatial analysis, three errors are computed: mean absolute deviation (MAD), median absolute deviation (MEDAD) and root mean square error (RMSE). In MAD, the deviation is greatly affected by outliers; in contrast, MEDAD values are much less sensitive to outliers. Fig 2.6 is obtained by calculating the MAD, MEDAD and RMSE values between the crossover differences and then averaged over the depth. From this figure, it can be seen that the MEDAD values are relatively lower than MAD which shows that there are some high errors in the attenuation rate. In Fig. 2.6(a)-(c) the MAD, MEDAD and RMSE values are scattered. The crossover differences are small for most of the crossovers. At the locations of larger ice thicknesses the attenuation rate differences at crossovers are higher. For larger thicknesses, the number of internal reflectors increases and to detect all the layers more reliably, it becomes more difficult hence resulting in high differences. The MAD and RMSE values are higher than MEDAD which means some high valued outliers are present in the differences. In terms of percentage errors these spatial errors are of order 22% for MAD, 15% for MEDAD, and 32%

for RMSE relative to the absolute values of attenuation rates. This also suggests that median values perform better because of the outliers in the results.

In the second analysis, again the same three crossover differences of MAD, MEDAD and RMSE are calculated at the crossover as a function of depth. Here, the attenuation differences are seen down the depth which shows that the differences are low at the top englacial layers and high at the bottom. This suggests that the deeper the englacier layer, the harder it will be to detect. Fig. 2.7 shows the attenuation rate over the depth for all the crossovers. The number of points contributing to the error calculations is also shown as a function of depth. The error at the ice base is high because detecting deep reflectors is difficult, the number of samples at these depths for crossovers is limited, and the absolute values of attenuation rates increases with depth. In terms of percentage depth errors the error increases with depth. Upto the depth of 800 m, the errors are under 29% for MAD, 24% for MEDAD, and 38% for RMSE relative to the absolute values of attenuation rates. As we go deeper the number of samples is also reduced and the deeper reflectors are harder to detect correctly so the error increases. Because of less samples at deeper depths, the uncertainty increases.

As discussed above, the minimum MSE occurs for the values range $0.3 \geq \lambda \leq 0.4$, which is shown in Fig. 2.3. We further explored which values will provide a more robust solution in context of crossover differences. The normalised median absolute deviation is plotted for all the crossovers as shown in Fig. 2.8 with different values of λ. In addition, these errors are averaged and is shown in Fig. 2.9. Both figures show the solution is more robust at $\lambda = 0.3$ and the attenuation rates result in values closer to typical reported values [39].

There are several reasons for discrepancies at the crossover differences. The crossovers can be from different field seasons and hence the physical situation

of the ice-sheet may differ and also small differences in equipment, result in varying radio echos. Another important reason is that ice is an anisotropic material [112] and the acquisition of radar data is from different flight path directions. For the majority of crossovers, the error values are low in comparison with the estimated attenuation rate values which implies the robustness of our proposed method. Also, to each cell in the 3D grid, there are many samples contributing to each cell which further reduces the uncertainty in the estimated attenuation rates.

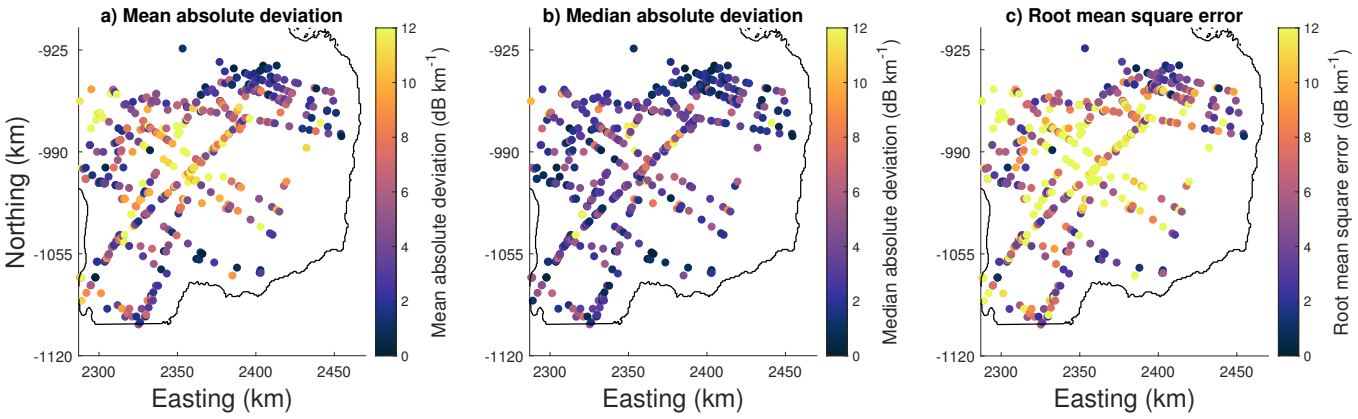

FIGURE 2.6: Each scatter point represents the crossover differences (mean absolute deviation, median absolute deviation, and root mean square error) averaged over depth. The median values are relatively lower than the mean which shows that there are few high error values which contribute to the mean errors which is also confirmed by high RMSE values.

2.5 Conclusions

In this paper, a new method for attenuation rate estimation is developed and used at the Law Dome region. The importance of this method is that it only relies on radar data and can be applied to regions where there is no information about the stratigraphy of englacial layers. We show that our method can be applied where

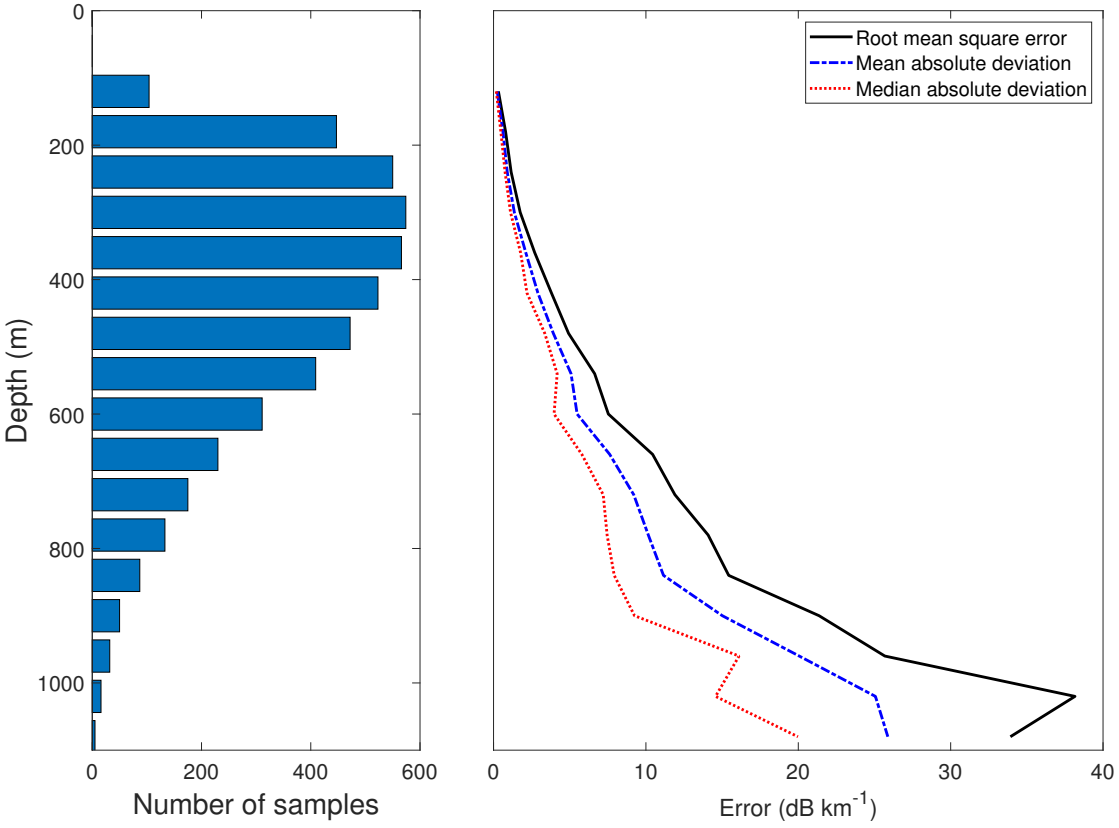

FIGURE 2.7: At crossover points, the figure shows different type of errors with depth. At each depth point, the corresponding error value is averaged over all spatial points. Here, the NaN values are discarded. Each depth value results from the different numbers of samples available at crossovers which is shown on the left side of the figure.

only radar data is acquired. This is an important advancement because from attenuation rates, the temperature profiles can be mapped, which could provide further insight into heat sources at the base of the ice-sheet (e.g. constraints on geothermal heat flux).

A high resolution attenuation rate can be obtained by this method with acceptable uncertainty and errors; however, it can be further improved by treating the assumptions made. Firstly, the quality of the estimated attenuation rates can be further improved if the actual strengths of the reflectors are used rather than assuming constant strength reflectors. Secondly, the ice anisotropy should be taken into account which is responsible for the different behaviour of radio waves when

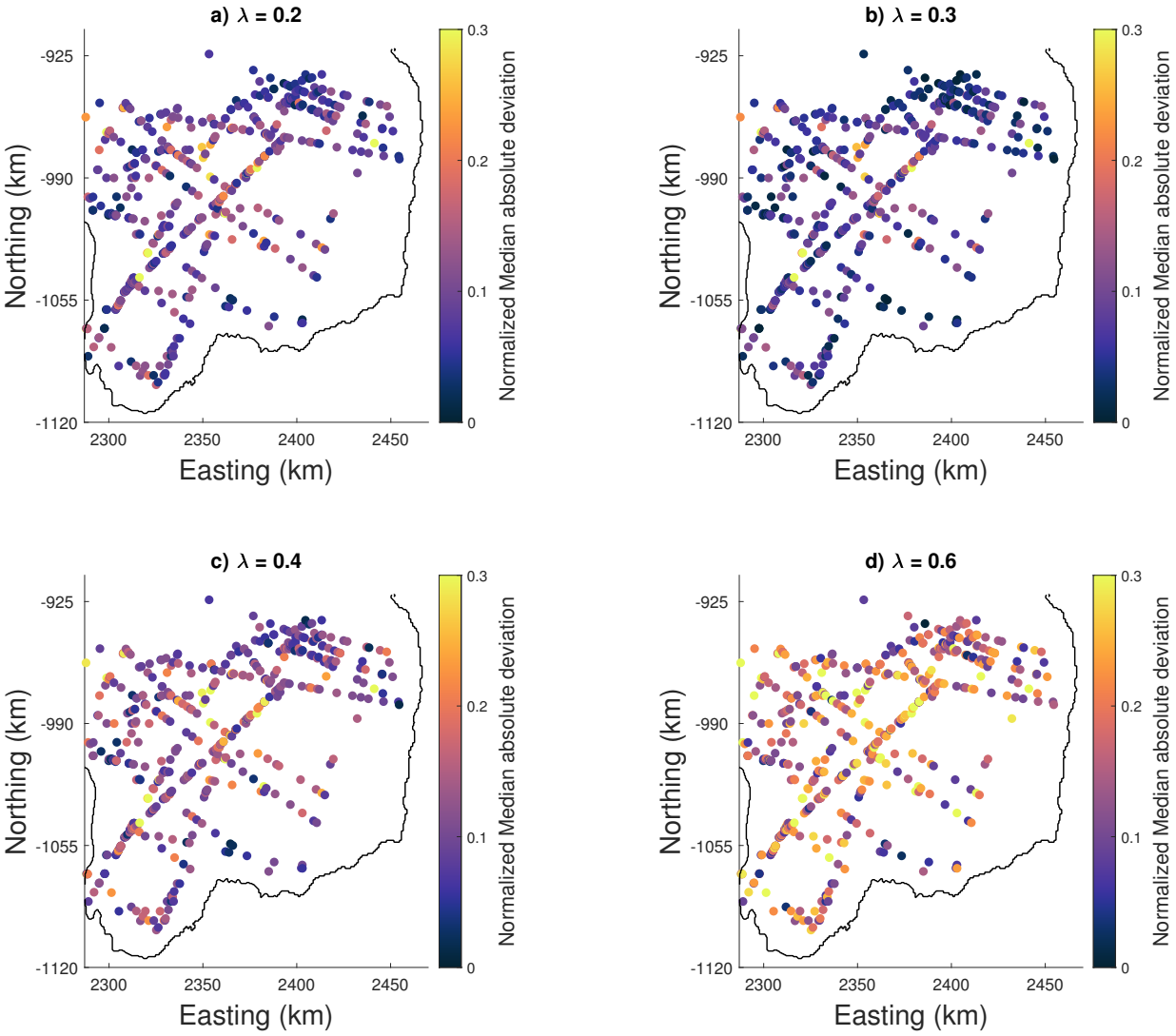

FIGURE 2.8: This figure shows normalised median crossover absolute deviation for different values of λ. The values for a) $\lambda = 0.2$ and b) $\lambda = 0.3$ are comparable but the values for $\lambda = 0.3$ is slightly small and resulting values closer to reported in literature [39]. As the values of λ increases, the normalised deviation for crossover increases, i.e., c) $\lambda = 0.4$ and $\lambda = 0.6$. Also note that the higher values of λ will force the resulting attenuation rates closer to zero and hence will be smaller than the typical values of attenuation rates.

incident on the ice from different directions. Finally, the automatic detection of internal reflectors can be further improved if the reflectors detected are traced in the adjacent ice columns or using prior information about the englacial reflectors using stratigraphy. However, in reality, the availability of such reflector information is

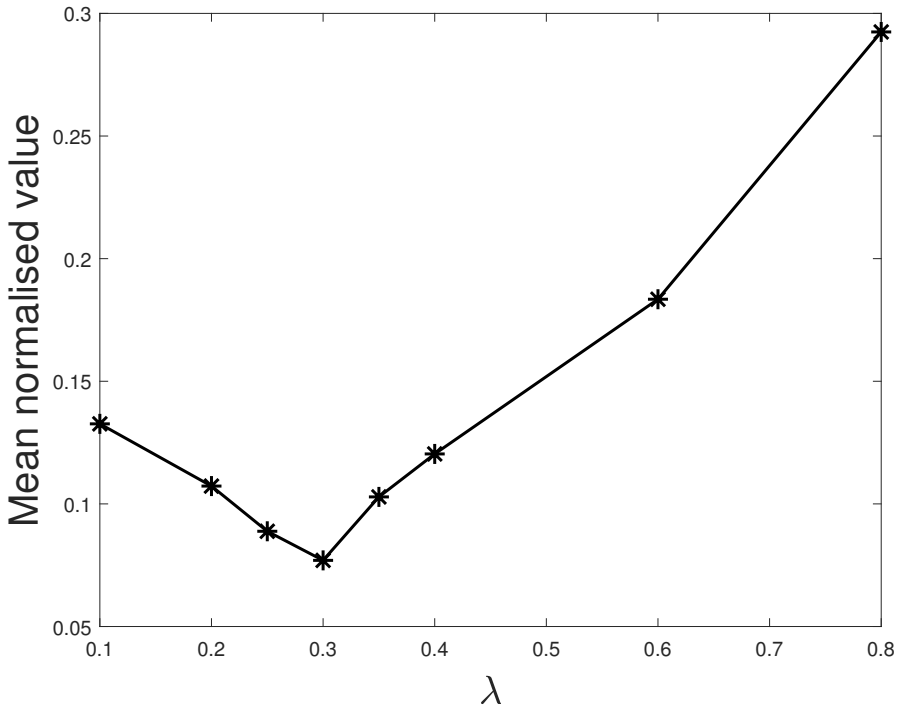

FIGURE 2.9: This figure shows the mean of the normalised attenuation rates for all crossovers shown in Figure 2.8. The minimum of the mean occurs at approximately $\lambda = 0.3$, which is our optimum value for robust solution.

very rare compared to the radar coverage.

Chapter 3

Temperature and Geothermal Heat Flux

3.1 Introduction

Within ice sheets, an understanding of the temperature distribution is important for knowing its intrinsic properties and other physical processes related to it. This is for a number of key reasons. Firstly, the deformation rate of ice strongly depends on temperatures as the viscosity of ice increases five times for a temperature decrease from -10 $Cto-25$C [9]. Secondly, rapid glacier sliding (which is one of the key processes that leads to ice mass flux into the oceans) occurs when the basal temperature approaches the pressure melting point and subglacial melt water is produced [9–11]. Finally, melt-water routes within glaciers can be affected by the ice temperature [9]. The interaction between ice flow and heat flow increases the complexity of ice dynamics and evolution substantially [9].

Geothermal heat flux (GHF) is a critical thermal boundary variable, strongly controlling the internal temperature distribution of the ice sheet and hence directly

influencing ice deformability and sliding [9]. Accurate geothermal flux estimates with sufficient spatial resolution are necessary to help reliably predict ice sheet evolution and future climate change [113]. However, direct measurements of temperature gradients from boreholes used to estimate GHF across Antarctica are limited and difficult to acquire [114–116], as most of the continent is covered by ice that is up to 4 km thick [4]. Instead, GHF datasets used in ice sheet models are commonly based on coarse geophysical magnetic data and seismic models [18, 117, 118].

This study infers the temperature distribution of the ice sheet and GHF across Law Dome using high resolution airborne radar data. Given the limited ice core temperature measurements, our methods have the potential to provide reliable temperature results to modellers and these methods can be extended to all of East Antarctica where extensive and spatially dense radar data sets already exist [84]. This will help to improve the knowledge of the temperature distribution within the ice sheet and GHF with high resolution and these results will contain high spatial frequency information which captures the underlying thermal regime well.

In Chapter 2, we derived a method for extracting attenuation rates from radar data. Here, this attenuation rate data is utilised to estimate temperature profiles at Law Dome. Later, the gradient of these temperature profiles is used to obtain GHF. The spatially varying GHF generated is very high resolution (1 km) as compared to previous results.

3.2 Background

GHF describes the movement of heat energy from the Earth's interior to the surface [119]. There are three main sources of geothermal heat: a) primordial heat

remaining from the Earth's formation; b) the latent heat released in the liquid outer core during crystallisation; and c) radiogenic heat produced by the decay of heat producing elements like uranium, potassium, and thorium [120, 121]. These radioactive heating elements are concentrated in the Earth's crust [122, 123].

In the past years, the basal thermal regime of ice caps, mountain glaciers and large ice-sheets has remained a subject of intensive research [13–15]. GHF is one of the major uncertainties in understanding the basal conditions of the Antarctic ice sheet. The estimation of Antarctic GHF is challenging because of the geological complexity of composite continental crust and only 0.2 % of the bedrock is exposed across the Antarctic ice sheet which makes direct access to the bedrock difficult [118]. Under the ice sheet, the spatial variability in GHF distribution is related to the geological evolution of the Antarctic continent, including variability in crustal heat production, heat from the mantle, crustal thickness, tectonic history, thermal conductivity, and volcanism [17–21, 124].

GHF strongly influences the ice sheet temperature affecting ice rheology, basal melt-water production, basal friction, sliding velocity, and erosion [17, 125, 126]. The heat energy conservation statement at the ice-sheet base is given by [127]:

$$G_{HF} + G_p + G_s + G_w + G_c + G_f + G_d = 0, \tag{3.1}$$

where G_{HF} is GHF, G_p is the heat required to maintain the water-flow at pressure melting point, G_s is the heat generated by sliding, G_w is the heat generated by subglacial water-flow, G_c is the heat conducted away towards the surface, G_f is the heat released by freezing or absorbed by melting, and G_d is deformational heat. Here, a positive sign of a component of $G(mWm^{-2})$ means the addition of heat to the system while a negative sign is removal of heat from the system.

GHF can be estimated from a) forward modelling of geological or geophysical data [18, 117, 118, 128–130], b) by inverse modelling of glaciological data [116], and c) temperature gradient of a borehole into bedrock or ice [93, 131, 132]. Geophysical methods derive the GHF from temperature—sensitive physical properties within the Earth's mantle or lithosphere. These geophysical methods include magnetic [18, 118, 133], seismic [117], and gravity modelling [134, 135]. To date, geophysical methods have been the predominant means of providing GHF maps at the continental-scale [18, 117, 118, 133]. The inverse modelling of glaciological properties like melt rates and glacial flow observations can also provide GHF estimates [136], but inverse models also require validation, particularly at the ice sheet base, which usually requires geophysical data.

GHF can also be estimated from the temperature gradient in boreholes. Measurements of temperature gradient and thermal conductivity in Antarctic bedrock or unconsolidated sediments is the most direct method to derive GHF. However, thermal gradients can be affected by processes other than GHF (including e.g., surface temperature and hydrothermal circulation) [115]. These processes can cause locally anomalous GHF estimates that may not be regionally representative. As most of Antarctica is ice covered so the use of ice-boreholes is another good method to estimate GHF from englacial temperatures. If the ice borehole measurements reach the bed, the temperature gradient can be calculated near the bed interface and GHF derived [131]. If ice borehole temperature profiles do not extend down to the bed, then the englacial temperature profiles or basal temperatures are reproduced to estimate the GHF with the compensation for heat diffusion [93, 132, 137].

Law Dome is dynamically stable (with relatively low velocities) and has minimal basal melting [23, 87]. In equation 3.1, this makes G_p, G_s, G_w, and G_f negligible at the base. It is also assumed that there is no deformational heat at the base

which makes G_d=0. The equation at the base of Law Dome thus becomes:

$$G_{HF} = -G_c, \tag{3.2}$$

which means the G_{HF} at the base is conducted away towards the surface.

In a recent study, the GHF estimate for Law Dome is 72 mWm^{-2} [137] while the previous estimate was 75.1 mWm^{-2} [23] which is about 4% higher. These estimates provide a single value for the entire Law Dome region (approximately 200 km in diameter). We know that GHF can vary significantly on spatial scales much smaller than this [138] and spatially varying GHF estimates can be obtained from continental scale GHF maps [18, 117, 118, 128]. Among these, only Martos et al. [118] provide a high resolution (15 km) GHF map. Other known GHF maps have hundreds of kilometres horizontal spatial resolution which is very low for a 200 km diameter region. While Martos et al. [118] might have 15km resolution, the GHF estimate varies smoothly across Law Dome (see Fig. 3.9) and does not show the shorter spatial scale variability modelled elsewhere in Antarctica [138]. The quality of continental scale GHF estimates strongly depends on local observations. For a region, if the number of observations are limited then the uncertainty is higher at that specific location in the continental GHF maps. None of the available GHF models cover Law Dome at high resolution. The aim here is to provide high resolution (1 km) spatially varying GHF estimates.

3.3 Methodology

This section discusses the two step process of estimating GHF from radar attenuation rates. Firstly, the attenuation rates are mapped to the englacial temperatures; secondly, the gradient of these temperatures is used to estimate GHF.

3.3.1 Attenuation Rates to Englacial Temperatures

This section develops a method for mapping attenuation rates (estimates derived in Chapter 2) to englacial temperatures. Radar attenuation is the loss (dB) of signal strength due to dielectric absorption, scattering and geometrical spreading. The attenuation rate is given by the following equation which describes the loss of energy from source to receiver per unit distance [97]:

$$N = \omega \left\{ \frac{\epsilon}{2} \left[\left(1 + \frac{\sigma}{\omega^2 \epsilon^2} \right)^{1/2} - 1 \right] \right\}^{1/2}. \tag{3.3}$$

The attenuation rate N strongly depends on σ electrical conductivity, ϵ permittivity and ω angular frequency. As σ and ϵ are strongly dependent on temperature, variations in the attenuation rate can be used to estimate englacial temperatures, subject to the assumption that the conductivity will remain the same. Also, the frequency bandwidth of the radar signal is narrow enough to assume that the attenuation rate will approximately remain frequency-independent (in the frequency range of VHF; 30-300 MHz) [26]. The radar data used here from ICECAP has a bandwidth of 15 MHz at the center frequency of 60 MHz [83].

In the past, Arrhenius temperature model is used to map attenuation rates to temperature profiles [26, 33, 65]. This model is very sensitive to conductivity. For Law Dome, conductivity data is not available rather a temperature profile is available [23]. Because of the high sensitivity of Arrhenius model in the absence of conductivity data we opted for mapping the actual temperature profiles. The Arrhenius model had been used in Greenland [26, 65] or West Antarctica [33]. In East Antarctica, Dome C has the acidity and sea-salt concentration data available [139], but Law Dome is a coastal region and sea-salt concentration may vary from Dome C. The Arrhenius function is too sensitive to these concentrations and it restricts us to use the temperature profile available at Law Dome.

Now, a mapping function is required from attenuation rates to englacial temperatures. To obtain this mapping function, the temperature profile from the ice-borehole at Dome Summit South (DSS) [23] and the attenuation rate data from Chapter 2 are used.

The only temperature profile to bedrock available at Law Dome is the DSS borehole. To utilise this profile more broadly across the whole Law Dome region, an assumption is made that the chemical properties of the entire region remain the same to rely on a single mapping function [33, 98]. Initially, an 8.5 km radius region is selected from the point of DSS to estimate a spatially averaged profile of attenuation rates which can then be used to obtain the mapping function. After obtaining the mapping function, the attenuation rates over the entire region are processed through this function to obtain the corresponding temperature profiles.

Generally, a high attenuation rate corresponds to higher temperatures. The attenuation rate changes with depth as shown in Fig. 3.1. The attenuation rates within an 8.5 km radius from DSS are shown at each depth level (each depth level is 60 m apart). It can be seen that some values are missing (represented by white grid cells) at each depth level. These missing values result either from not detecting the englacial layer at that depth level (by our method) or the flight line not passing within 500 m of the grid cell. From the attenuation rates pattern it can be seen that the attenuation rates increase with depth which is also the case with temperature profiles as discussed above.

The data within 8.5 km of DSS is used to generate our required attenuation rate profile which will be used to construct the mapping function. This radius is selected as it provides enough points for generating mapping function. If we select higher values for the radius, it will diminish the robustness of the mapping function (extrapolation issues). The reason we selected this radius is that it was smaller

enough to have sufficient data points at different englacial layer depths. We sometimes have missing reflectors which means that for smaller radii we will not have enough points at each englacial reflector and missing points at some reflectors is not good for deriving the mapping function. At each depth level, the median value of attenuation rate is selected. As from Chapter 2, the median value is robust for our algorithm because of the possible outliers in the results. Fig. 3.2 shows the median values at each depth level and the number of samples contributing to each depth level is also shown in the bar chart. The attenuation rate increases with depth except at 1140 m (note that the DSS ice thickness is approximately 1200 m [87]). This is because the deepest reflectors are hard to detect. In addition, the number of samples at the last reflector is small which makes it relatively unreliable. The attenuation rates monotonically increase up to 1080 m which means that the englacial temperature increases with depth. The higher the number of samples, the more reliable the results because we have enough samples at those depth levels. From this trace of attenuation rates we can rely on the estimated attenuation rate up to 1080 m which is above the base by over a 100 m (see section 3.3.2).

The attenuation rate trace obtained at DSS is mapped against the ice-borehole temperature profile at DSS as shown in Fig. 3.3 to fit the mapping function. We are more interested in correctly mapping the deeper attenuation rates, as it will be utilised for estimation of GHF (derivative of temperatures). The top layer temperatures do not vary much up to certain depth (approximately 500 m) and then increases with further depth as shown in the Fig. 3.3. On the other hand, the attenuation rates are increasing continuously right from the surface as shown in the Fig. 3.1. The depth sampling is 60 m so we have depth samples at 0 m, 60 m, 120 m, ..., 480 m, ..., 1200 m, among this sequence, 480 m is the closest to 500 m. The starting sample for generating the mapping function is 480 m and the last

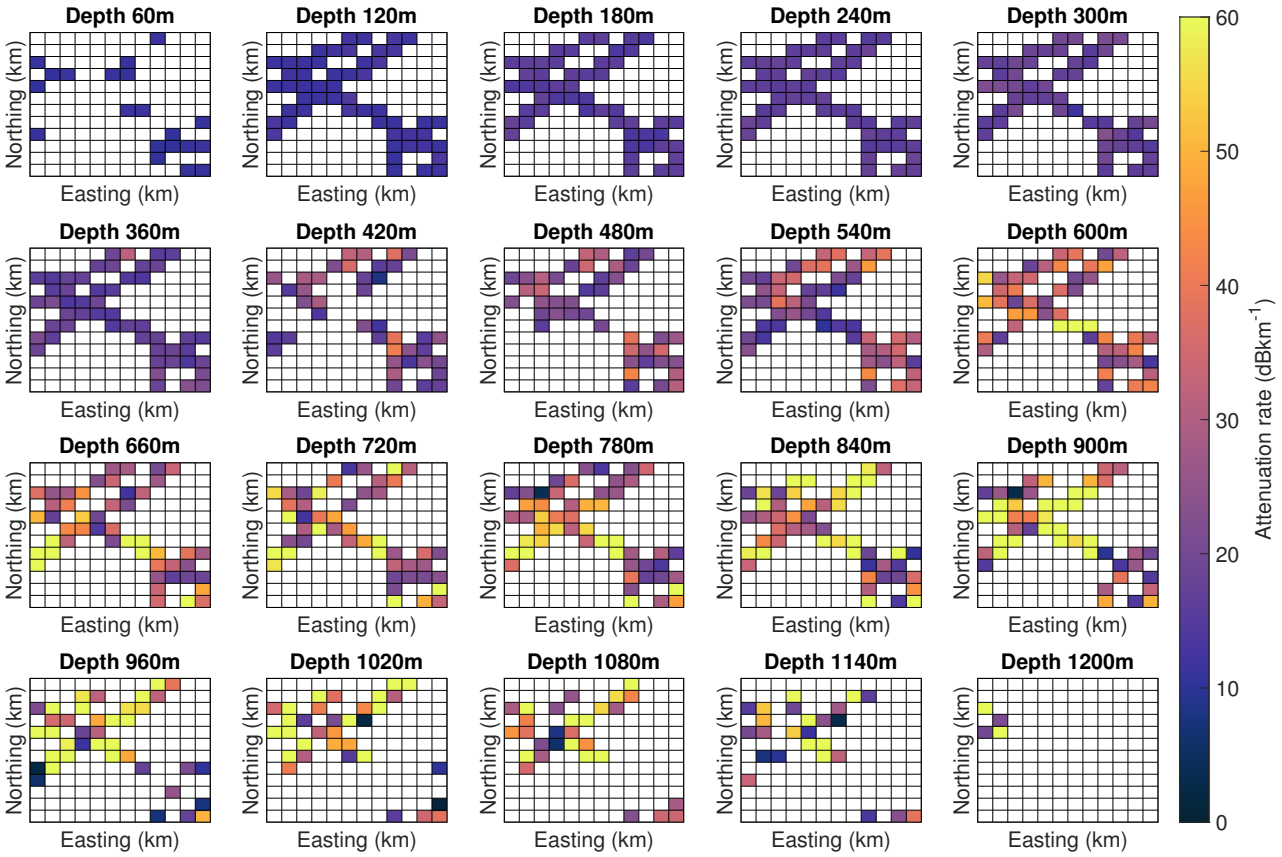

FIGURE 3.1: Attenuation rates at different depth levels at DSS within 8.5 km radius. There are a total of 20 depth levels shown in the figure, each frame is a depth level and corresponding depth is shown in its title. In each frame, there are a total of 12 x 12 grid cells, each grid cell corresponds to approximately 1 km x 1 km. The centre of each frame is at DSS. This figure also shows the trend of attenuation rates which increases with depth.

sample is 1200 m (the maximum depth). If we use the upper layers temperature for mapping, it will bias the Attenuation-Temperature mapping and will result in a function which will not capture the actual Attenuation-Temperature relation at the deeper layers (the layers important for estimating GHF at the base). The mapping function is shown in Fig 3.4 is obtained by fitting a least squares function. The mapping function is given by equation:

$$T = p_1 N + p_2, \tag{3.4}$$

where $T(^{\circ}C)$ is the output temperature for a given attenuation rate $N(dBkm^{-1})$, derived constants are $p_1 = 0.4411$, and $p_2 = -35.45$. This function is utilised to transform the attenuation rate data generated in Chapter 2 to temperature profiles which are used in the estimation of GHF as discussed in the next section. The deeper the englacial reflector the harder it is to detect it reliably. In our method the deepest reflector is not always at the base as sometimes it is not reliably detected. This causes a problem in estimating the temperature exactly at the base, although extrapolation can be used to estimate the temperatures at the base. Here we are more interested in the gradient of temperatures and a correction mechanism is developed if the deepest reflector detected is not at the exact base.

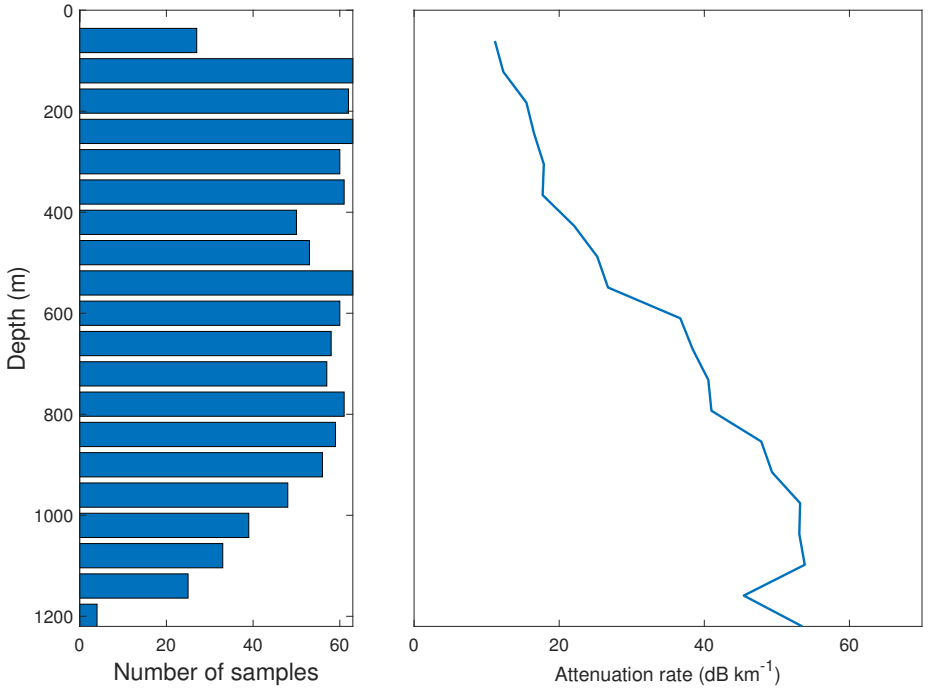

FIGURE 3.2: Median of attenuation rates within 8.5 km of DSS at each depth level. The left side shows how many samples at each depth level are contributing to the median value and the right side of the figure plots the median values of attenuation rates at each depth level. Depth levels are 60 m apart and 0 m reference is from the ice surface.

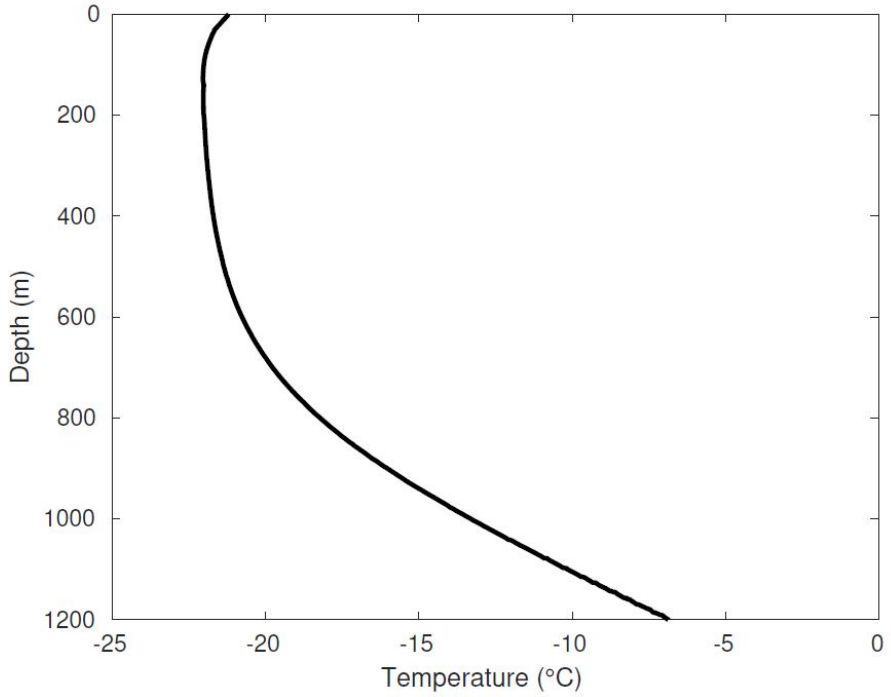

FIGURE 3.3: Temperature profile at Law Dome DSS borehole site [23].

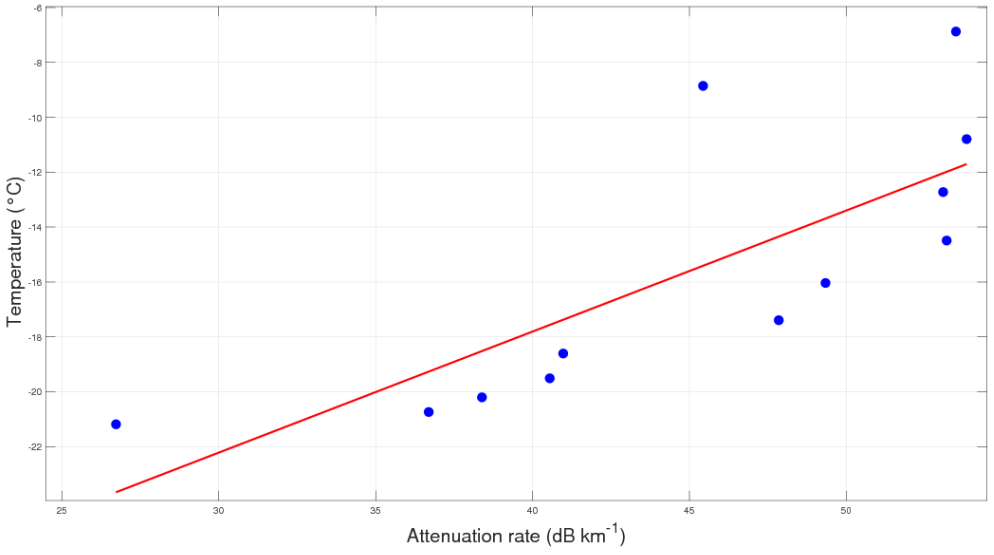

FIGURE 3.4: Fitting the curve to obtain attenuation rate to temperature mapping function. For fitting the curve, the temperature and attenuation rate points are selected from depth 480 m to 1200 m.

3.3.2 Calculating geothermal heat flux from temperature gradient

From the previous section, the temperature profiles along the ice-column are available and the gradient of these temperature profiles is utilised to calculate the GHF. According to Fourier's law in one dimension the heat flux q can be calculated from the temperature gradient [118] as:

$$q = -k\frac{dT(z)}{dz}, \tag{3.5}$$

where thermal conductivity for ice is $k = 9.828\ exp(-0.0057\ (T(^{\circ}C) + 273.15))$ $(Wm^{-1}K^{-1})$ [140]. This equation can give us GHF at the base if we have a temperature profile down to the base. However, the temperature profile we obtained was down to certain depths which were slightly above the base. In regions of accumulation, the temperature gradient increases with depth (the maximum gradient is at the base) [9]. If our deepest reflector is not exactly at the base, we need a compensating correction mechanism.

In glaciers, heat is conducted both vertically and horizontally, but the horizontal part is usually negligible because of its smaller temperature gradient. In addition, we are near an ice dome, and hence the horizontal velocities are low and horizontal advection can be neglected. However, the vertical advective heat transfer by means of ice flow is important [9].

The following equations describe the dimensionless quantities, which are later used in the correction mechanism of heat flux. The dimensionless distance above bed is given by:

$$\xi = \frac{z}{H}, \tag{3.6}$$

where z is distance above bed and H is the ice thickness. The dimensionless temperature is

$$\Theta = k\frac{(T - T_s)}{GH}, \tag{3.7}$$

where T_s is temperature at the surface and G is GHF. At the bed, the temperature difference between surface and the bed is given as [9]:

$$\Theta_B = \left[\frac{\pi}{2\gamma}\right] erf(\gamma/2)^{1/2}, \tag{3.8}$$

where

$$\gamma = \frac{\dot{b}_i H}{\alpha_T}$$

is the advection parameter [9], $\dot{b}_i$ is accumulation or ablation rate, H is ice sheet thickness, and α_T is Thermal diffusivity. The γ is positive for accumulation and negative for ablation regions. The γ is similar to the *Péclet Number* which also indicates the relative importance of advection to conduction [9]. At DSS, the value of γ is 10.65. The increase in temperature gradient towards the base is a consequence of the decreasing vertical velocities of ice, and hence a decreasing advective heat flux. Fig. 3.5 summaries the effect of γ in terms of dimensionless temperature and height from the bed. When $\gamma = 0$, it means that the temperature gradient remains constant from the surface to the bed. When $\gamma > 0$ (corresponds to accumulation), the temperature gradient is increasing from the surface to bed. When $\gamma < 0$ (corresponds to ablation), the temperature gradient is decreasing from the surface to bed. Here in the case of Law Dome the value of γ is positive. The RACMO2 data will be utilised for accumulation rates [141].

The temperature gradient is estimated at the deepest reflector detected by our method. The temperature gradient is high at the base in the accumulation regions. Initially, the conductive heat flux is estimated using least squares for the

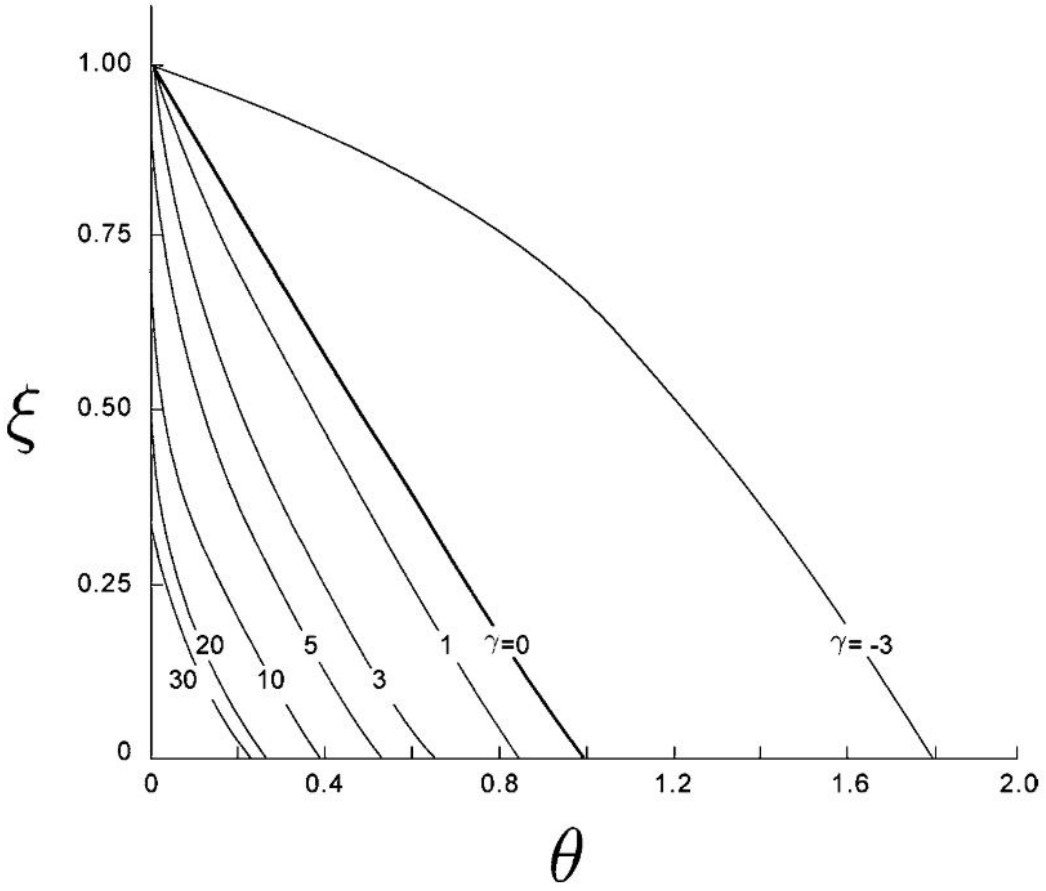

FIGURE 3.5: Dimensionless steady-state temperature profiles for different values of advection parameter γ. For positive values of γ the gradient is highest at the bed and the gradient changes depending upon the value of γ while for negative value of γ the gradient is the smallest at the bed. The figure is from Chapter 9, The Physics of Glaciers [9].

temperature gradient $\frac{dT(z)}{dz}$, the slope in the fit is used to estimate the conductive heat flux at the deeper reflectors. The deepest reliable reflector detected by our algorithm is approximately 100 m above the base. Using the methods described above, we estimate a conductive heat flux of 63.2 mWm^{-2} at 100 m above the ice sheet base. This is less than the GHF of 72 mWm^{-2} estimated at Law Dome [23, 137]. The difference between the two GHF estimates is used to compensate for the heat flux. The accumulation rate, our deepest reflectors and ice thickness varies spatially; so, this compensation is required to apply to the whole region spatially trace-by-trace.

We assume all other heat fluxes are negligible for this region, that within the ice

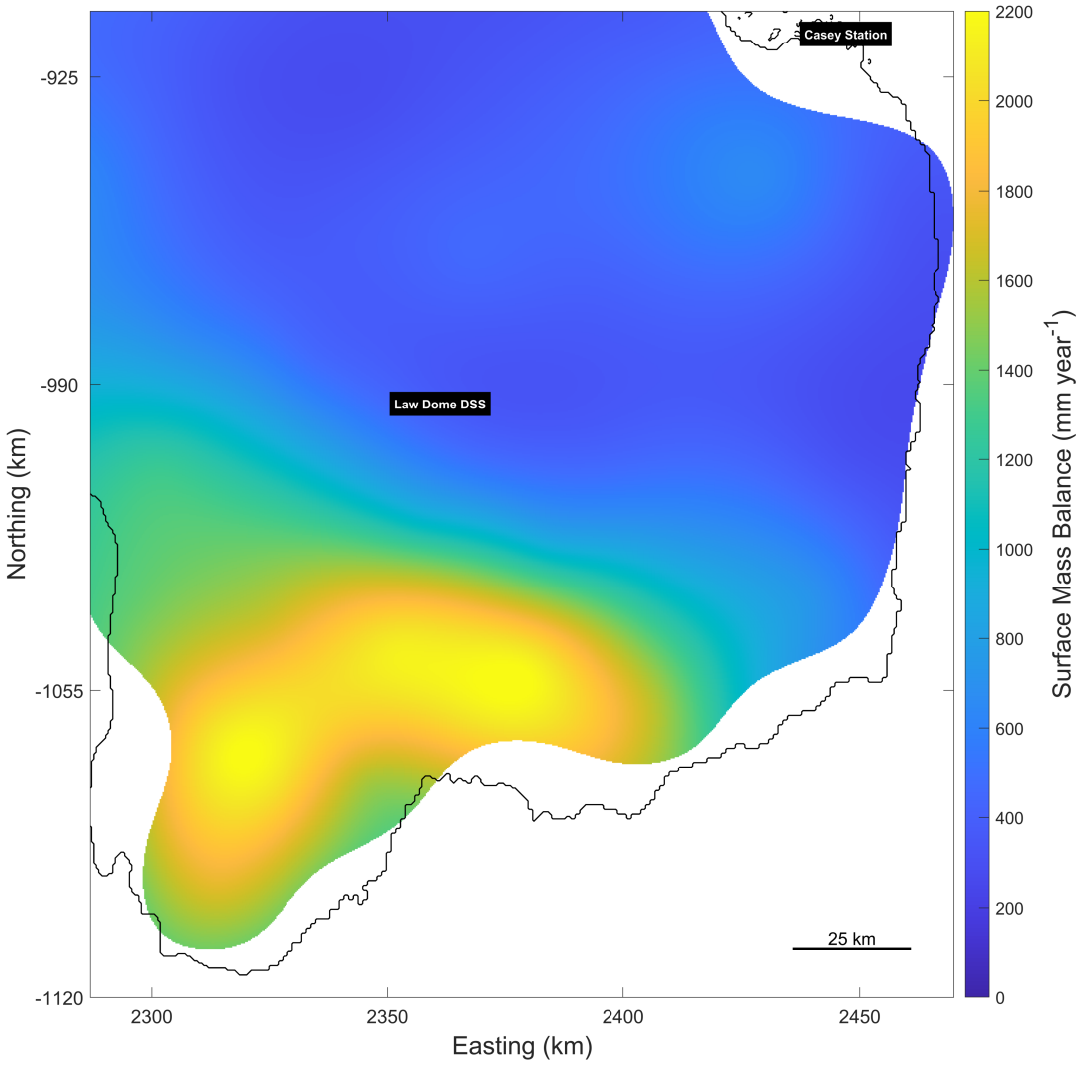

FIGURE 3.6: The RACMO2 surface mass balance data is used for correcting the advective component of heat flux [141]. Bilinear interpolation is used to smooth the data as the original data resolution was too low for our requirement [142].

the sum of the vertical advective and conductive fluxes must be constant, and that for positive accumulation regions the advective flux decreases with depth and is zero at the base (for regions without basal melt). At the base of the ice, the GHF is equal to the conductive heat flux in the ice. If the deepest detected reflector is above the base, we need to estimate the advective heat flux component and add this to the calculated conductive heat flux to estimate the total heat flux within

the ice. For the correction of the advective component, the surface mass balance data is used as shown in Fig. 3.6. The following steps summarise the advective correction made in this study:

Each trace advective component is calculated based on the two values, how much the detected reflector is above the base and how much is accumulation rate there. We assume that the ratio of accumulation rate at DSS is equal to the ratio of γ. For a steady ice sheet elevation, the vertical velocity is in balance with the snow accumulation, so that the advective heat flux will scale with the accumulation rate. We scale this advective flux at DSS by the ratio of the local snow accumulation rate to the accumulation rate at DSS (using RACMO2) [141]. Using the values of relative depth and the scaled advective flux, the advective heat flux component at corresponding depth reflector is calculated. The final corrected GHF is simply the addition of the conductive and compensating advective heat fluxes.

3.4 Results and Discussion

In this chapter, the attenuation rates are mapped to temperature profiles which are later used for GHF estimations. Here, we show the temperature at the deepest reflector detected by our algorithm. Fig. 3.7 shows the ice thickness [3], deepest reflector detected, and the temperature closest to the base detected by our method. From Fig.2.5, it can be seen where the temperatures are more reliable. In some places the number of estimated attenuation points are very limited and will result in poor approximation. Also, when we get closer to the coast the ice thickness decreases and the reflector detection capability also decreases in the firn; so, the resultant temperatures are not very reliable here (approximately 10 km from the

coast). The temperatures are more reliable in the centre part of the figure because of more estimation points and higher thickness. At DSS, the reported basal temperature is approximately $-7\ ^oC$ [23].

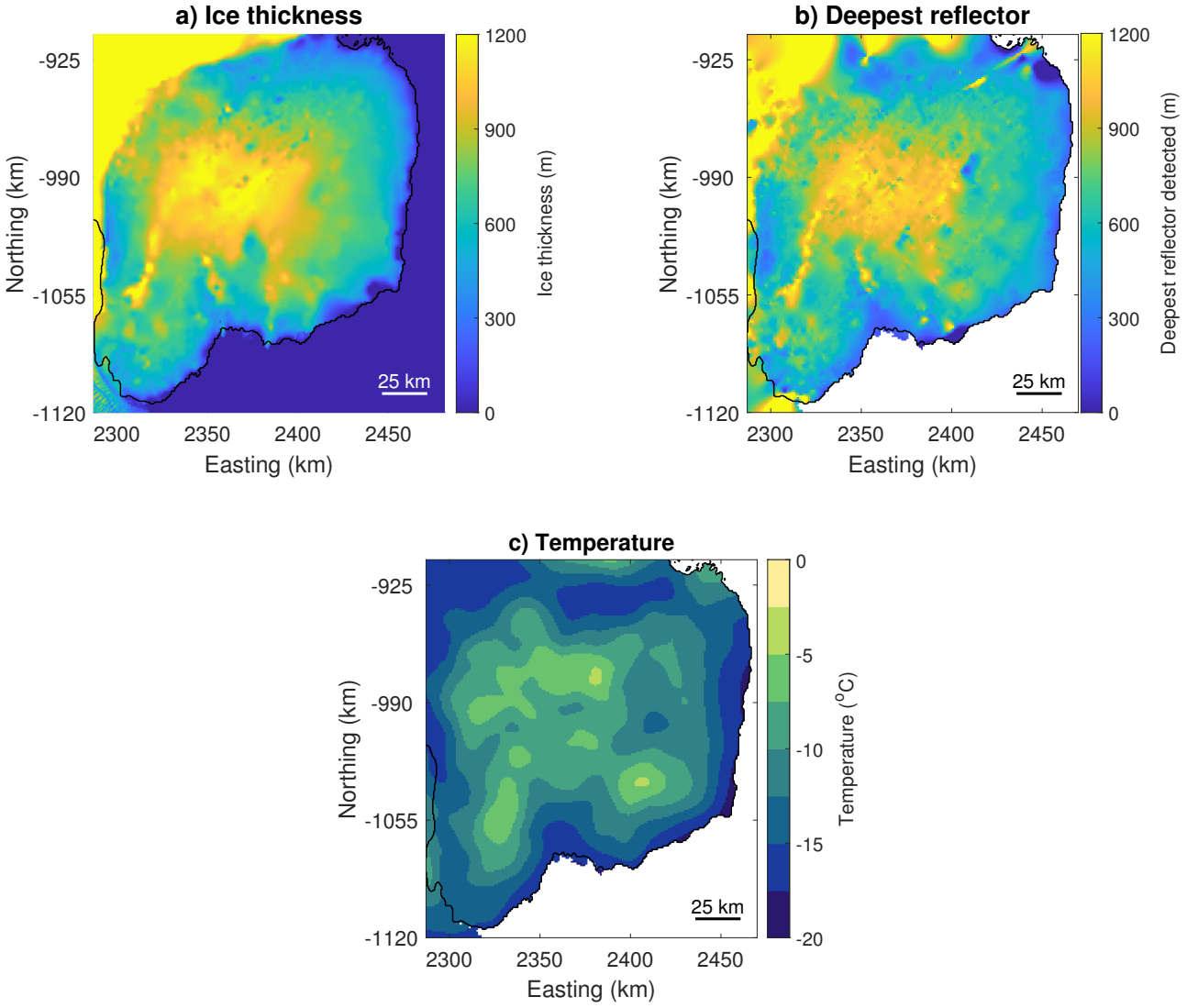

FIGURE 3.7: a) Ice thickness [143]. b) Deepest reflector detected by our method. c) Temperatures at these detected deepest reflectors.

We also obtained two estimates of GHF: the first one is before correction and the second one is after vertical advective correction. The advective component is dependent on the accumulation rate of the ice. Annual average (1979–2014) RACMO2 accumulation rate data is used for this purpose [141]. The resolution of

accumulation rate data is too coarse, therefore a bilinear interpolation was applied to sample the RACMO data at each radar trace.

The RACMO uncertainty or error in bilinear interpolation contributes to only the advective component of heat flux (8.8 mW/m2), which is only 12.2 % of the total GHF. The main component which is conductive component derived from radar is 87.2 % and it is not affected by RACMO. The RACMO uncertainty is translated linearly because of the linear relation in our correction method. For instance, if RACMO has 30 % uncertainty, it will only contribute 3.7 %, which is not that high as compared to the uncertainty in our derived attenuation rates shown in the Fig. 2.4.

Fig. 3.8 shows the GHF before correction which is purely dependent on the temperature gradient and after correction to compensate for the advective flux. The advective component contributes more where the value of γ is higher as shown in Fig. 3.5. Here at Law Dome the value of γ is positive. The results are interpolated using bilinear interpolation within the grid using gradient regularisation and solving it as normal equations [142].

In Fig. 3.9 the GHF models from previous methods are shown across Law Dome. Fig. 3.9a and 3.9b show the Shapiro and Ritzwoller [117] and An et al. [128] seismic estimate of GHF respectively; panels c and d show the magnetic models Maule et al. [18] and Martos et al. [118] respectively. These methods provide GHF coverage over Antarctica. The spatial resolution of GHF by Shapiro and Ritzwoller [117] is 600-1000 km, Maule et al. [18] is approximately 200 km, An et al. [128] is approximately 120 km, and the Martos et al. [118] method produces GHF of relatively higher horizontal spatial resolution—15 km. The GHF fluxes in each case are lower than the ice borehole estimate of 72 mWm^{-2} [23, 137]. The Martos et al. [118] estimate is the highest of the datasets and closest to the

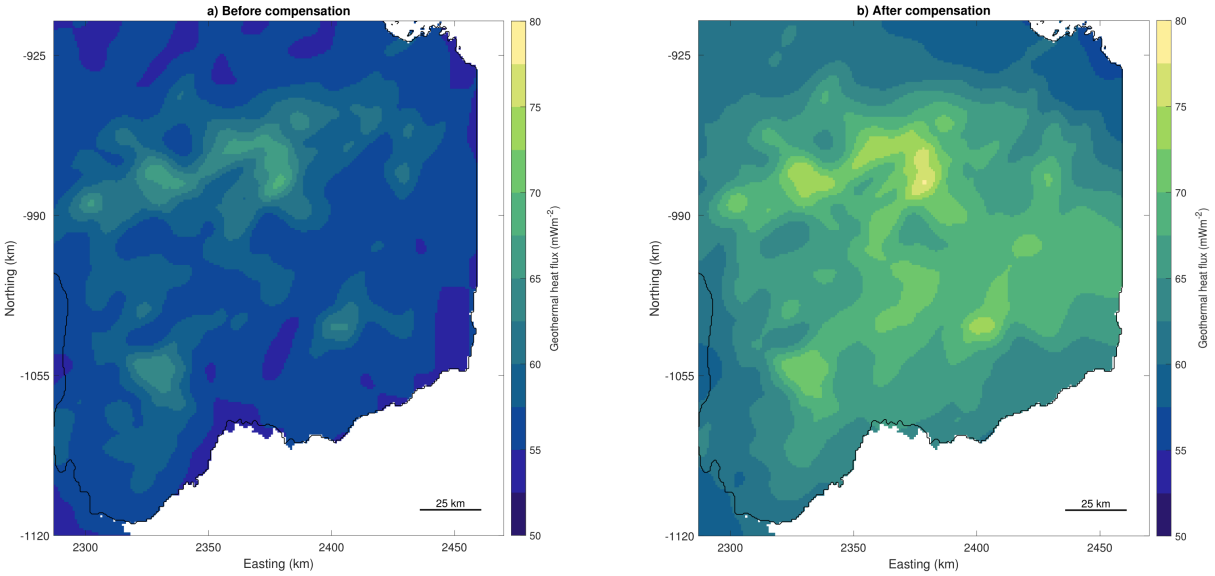

FIGURE 3.8: a) GHF across Law Dome before advective correction which is purely obtained from temperature gradient. b) GHF after the correction term is added which compensates for the advective term above the bed.

borehole estimate. When the advective compensation is applied to our estimate, the GHF across all of Law Dome is in the range 65-80 mWm^{-2}.

There are a number of assumptions that impact the uncertainty associated with our GHF estimate. We are relying on a single ice borehole temperature profile which makes our method extremely sensitive to the measurements of those borehole temperature profiles. If these measurements have a high degree of uncertainty, it makes our mapping function less certain. We also assumed that the impurities (acidity etc.) at Law Dome over the entire region remains constant. In places where there is high spatial variability in chemical properties over relatively short distances, this will decrease the robustness of our method.

We used a basic correction mechanism for GHF. There is an alternative way to deal with this compensation. For example, Zagorodnov et al. [93] used a numerical method which extrapolates the temperature profiles down to the bed. From here, the temperature gradient was estimated right at the base, which is proportional to GHF assuming there is no other heat source or sink. Such a method circumvents

the need for an advective correction. In our case the spatial and vertical resolutions are very high and the temperature profiles are not very smooth in the adjacent grid cells (also we have different detected depth layers) which may lead to poorer extrapolation.

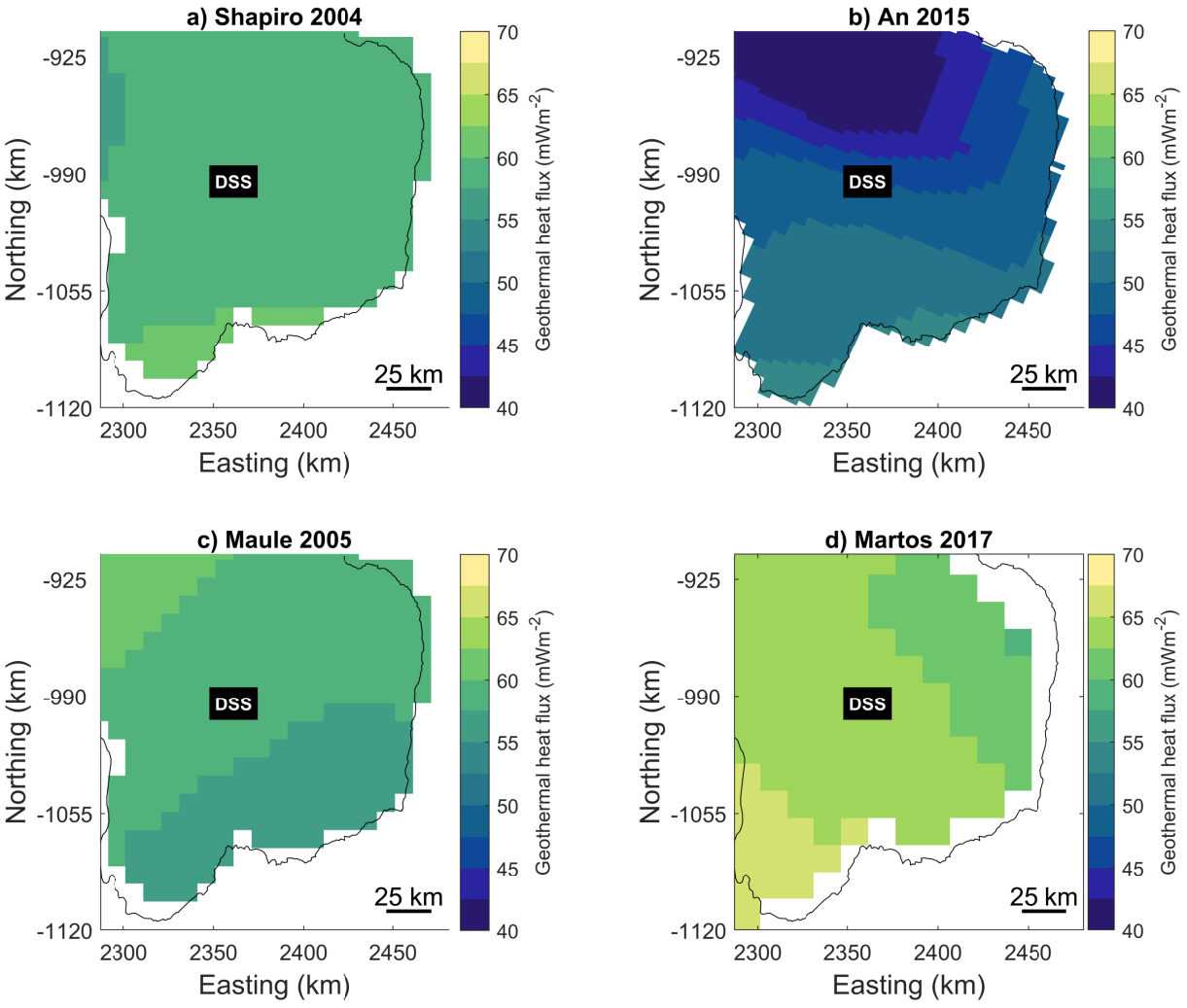

FIGURE 3.9: GHF across Law Dome using seismic model estimate (a and b; [117, 128]) and magnetic methods derived from Curie depth estimates (c and d; [18, 118]). Among these methods, Martos et al. [118] is the only high resolution GHF estimates on continental scale.

3.5 Conclusion

In this chapter, the attenuation rates obtained in Chapter 2 are used to estimate englacial temperature and GHF for the Law Dome region. A method is developed which transforms the attenuation rates into temperatures using a mapping function. This mapping function is obtained by using the actual temperature profiles from the DSS borehole. It is assumed that this mapping function will remain the same throughout the region. Here only one profile was available; however, where multiple ice cores temperature profiles are available, all can be utilised to obtain this mapping function.

The temperature profiles are further processed to obtain the GHF. GHF obtained through our method resulted in a smaller value at DSS than the previous estimate. Since the radar sounder does not always detect the deepest basal ice reflector, a correction for the advective heat component must be applied. So, we will have two heat flux components, i.e., conductive and advective (corrective compensation). The conductive part is obtained using a 1D Fourier heat flux equation, while the advective part is corrected and added to the heat budget based on the difference between our estimate and direct calculations of GHF at DSS.

Our method is applicable to other regions where we have at least one temperature profile, radar reflection data, ice thicknesses and annual accumulation rates. The benefit of this method is that, being derived from high-resolution radar data, it provides very dense spatial resolution results, on the order of a kilometre, which is particularly relevant in regions of Antarctica where local highs in GHF may significantly impact the dynamics of ice flow.

Chapter 4

Conclusions

In this thesis, a radar-based method is developed for estimating the attenuation rates, then these estimates are used to obtain temperature profiles. The gradient of these englacial temperatures is used to generate a GHF map across Law Dome. For attenuation rates, the returned power is first corrected for geometrical path loss. After this correction, the most important step is to detect the englacial layers correctly. The problem is then mathematically formulated as a constraint regularised l_2 minimisation problem. Solving the minimisation problem leads to the englacial attenuation estimates. In the next step, these attenuation estimates are mapped to englacial temperatures using a mapping function. The mapping function is obtained using ice borehole temperature profile at DSS. The mapped temperature profiles are used for estimating GHF from temperature gradient. In the final step, a corrective compensation mechanism for GHF estimates is conducted to get our final GHF estimates across Law Dome.

In Chapter 2, we used raw radar data from ICECAP project over Law Dome to estimate the attenuation profiles using our method. A 3D attenuation rate dataset is generated using this method which is 1 km x 1 km x 60 m. This means that the horizontal spatial resolution is 1 km x 1 km and the vertical resolution along

the depth is 60 m. The depth-averaged attenuation rates along with uncertainties are provided. To validate our method, crossover analysis was conducted both spatially and along the ice-column. There are a total of 582 crossovers (crossover is considered within 35 m). In spatial analysis of crossovers, three differences are computed, i.e., mean absolute deviation (MAD), median absolute deviation (MEDAD), and root mean square error (RMSE). Spatially, these differences for crossovers are relatively small as compared to the absolute values of attenuation rates which means that our method is robust. Along the ice-column the same MAD, MEDAD, and RMSE differences are calculated. Among these errors again the MEDAD is the smallest. As the depth increases, the values of these differences increases because the deeper the reflector, the harder is the englacial layer detection which leads to higher error differences. In both spatial and depth crossover analysis the values of MEDAD are relatively less which means that our estimates contain some outliers. The method is fully automatic and some bad radar traces might lead to outliers. To minimise the effect of outliers, median values were selected while generating the final 3D attenuation rates map. The depth-averaged attenuation rates are higher at regions where ice is thicker. Similarly, the uncertainty in attenuation rates is also higher at thicker regions because englacial layer detection at deeper regions is relatively a more difficult task.

In Chapter 3, we used ice borehole temperature profile data to transform the attenuation rates from Chapter 2 to temperature maps. A mapping function is required to transform the attenuation rates to temperatures profiles. This mapping function is generated using the ice borehole temperature at DSS [23] and the median values of attenuation rate within radius of 8.5 km from DSS at each depth level. From the temperature gradient, we estimated the conductive GHF and a correction term is added to compensate for advective component which leads to our GHF estimates. Our conductive flux estimates are 8.8 mWm^{-2} lower from the

previously reported value [137]. These estimates are lower because of our deepest englacial reflector is not the base. A correction term of advective heat flux is calculated using RACMO2 accumulation rate data over Law Dome and is added to conductive flux to get our final GHF estimates.

The temperature mapping function is obtained using only a single borehole site and considering the ice chemistry to remain the same throughout the region. If the chemical properties change rapidly over the spatial region then this mapping function will not capture the actual relation. In addition, this mapping function is a first order linear function. In reality, this is not a first order relation but we selected this approach as we had very limited points to generate this mapping function. The higher order relations require more points to avoid over-fitting.

This method can be applied to regions where radar data and ice-borehole temperature profile is available within a few hundred kilometres. We applied this method to a relatively small region of approximately 200 km diameter which is stable and slow-moving. On the continental level, it needs to be investigated how the methodology performs in more complex topography and fast-moving regions. We already know that the method performance degrades when the ice thickness increases. If the method is expanded on continental scales then the crossover analysis should also be performed over regions of larger ice thicknesses. It should be also be taken into account that whether the method is correctly detecting englacial layers over a variety of terrains across the continent. If the method is applied on larger regions having multiple ice-borehole profiles, then regional attenuation-temperature mapping functions will be more suitable.

Most of the previous methods extract an depth-averaged value of attenuation rates and also requires information about englacial layers reflectivity and its depth location. Our method is a complete path to get GHF from raw radar data and a single column of the ice sheet temperature profile.

Future Directions

In our method, we assumed that the englacial layers are considered to have the same reflective strength which is not the case in reality. If the englacial layers reflectivity is provided then corresponding correction will improve the attenuation estimation. In addition, stratigraphy of englacial layers can cross validate our automatic englacial layers detection method. On continental scales stratigraphy is a complex process but if available for certain regions then it can be helpful in tuning the method [144–147]. In our method we processed radar data column by column and the detection process can be further improved if the englacial reflectors are traced within the adjacent columns [144]. As the deeper reflectors are hard to detect in the current method, the tracing within the adjacent columns will improve deeper detection which can help expanding the method to continental scale [26].

Mapping from attenuation to temperature assumes the same chemical properties throughout the region [26, 34]. If spatial variation in ice chemistry is embedded in the mapping function, it can further improve the mapping function which will not require the assumption of same chemical properties; however, it will require substantial amount of chemical information of the region. In addition, if we have more than one borehole for certain regions, it can help in improving this mapping function. A high order mapping function is better to capture that actual physical relation between temperature and attenuation rate but more data points are required to generate this high order mapping function. More temperature profiles means more data points for mapping function.

In estimation of GHF, the correction for advection is treated in a very basic way [9]. An alternate approach can be to improve the englacial layer detection process to detect the deepest reflector correctly. Once we have that reflector there will be no need of this correction because we will have temperature profiles up to the bed.

This method can be applied to other regions of interest where radar data is available [84, 104]. If temperature profiles are not available, only attenuation rate data is also helpful in correction of radar returned power. In addition to radar data if temperature profiles are also available [23, 93], then we can obtain GHF maps over that region from raw radar data. There is plenty of radar data available over Antarctica [3, 84, 104].

Accurate estimates of englacial temperature and geothermal heat flux are incredibly important for constraining model simulations of ice dynamics (e.g. viscosity is temperature-dependent) and sliding [9]. However, we currently have few direct measurements of vertical temperature (i.e. only at boreholes/ice domes) [22–25] and geothermal heat flux in Antarctica [18, 117, 118, 128]. This method derives attenuation rates, that can then be mapped directly to englacial temperatures and geothermal heat flux. A novel approach is developed which uses the radar sounding data to estimate these temperatures and GHF. If we compare the existing GHF maps [18, 117, 118, 128], they have much lower resolutions as compared to what is offered by our method as the acquisition of airborne radar data is normally very dense [3]. In addition, a mapping function is required which can be generated either from temperature profiles or using Arrhenius function by utilising chemical properties (i.e. acidity and sea-salt concentrations) of the region [33, 34]. By doing so, a higher resolution GHF map is possible on continental scale.

Bibliography

[1] S. Abdul Salam. A 3D map of englacial attenuation rate from radar reflections at Law Dome, East Antarctica. 2020. doi: 10.25959/5e6851e266f4a.

[2] T. F. Stocker, D. Qin, G. K. Plattner, M. Tignor, S. K. Allen, J. Boschung, A. Nauels, Y. Xia, V. Bex, and P. M. Midgley. Contribution of working group I to the fifth assessment report of the intergovernmental panel on climate change. *Climate change*, 2013.

[3] M. Morlighem, E. Rignot, T. Binder, D. Blankenship, R. Drews, G. Eagles, O. Eisen, F. Ferraccioli, R. Forsberg, P. Fretwell, V. Goel, J. S. Greenbaum, H. Gudmundsson, J. Guo, V. Helm, C. Hofstede, I. Howat, A. Humbert, W. Jokat, N. B. Karlsson, W. S. Lee, K. Matsuoka, R. Millan, J. Mouginot, J. Paden, F. Pattyn, J. Roberts, S. Rosier, A. Ruppel, H. Seroussi, E. C. Smith, D. Steinhage, B. Sun, M. R. van den Broeke, T. D. Ommen, M. van Wessem, D. A. Young, T. D. van Ommen, M. van Wessem, and D. A. Young. Deep glacial troughs and stabilizing ridges unveiled beneath the margins of the Antarctic ice sheet. *Nature Geoscience*, 13(2):132–137, 2020. ISSN 1752-0908. doi: 10.1038/s41561-019-0510-8.

[4] P. Fretwell, H. D. Pritchard, D. G. Vaughan, J. L. Bamber, N. E. Barrand, R. Bell, C. Bianchi, R. G. Bingham, D. D. Blankenship, G. Casassa, G. Catania, D. Callens, H. Conway, A. J. Cook, H. F. J. Corr, D. Damaske, V. Damm, F. Ferraccioli, R. Forsberg, S. Fujita, Y. Gim, P. Gogineni, J. A.

Griggs, R. C. A. Hindmarsh, P. Holmlund, J. W. Holt, R. W. Jacobel, A. Jenkins, W. Jokat, T. Jordan, E. C. King, J. Kohler, W. Krabill, M. Riger-Kusk, K. A. Langley, G. Leitchenkov, C. Leuschen, B. P. Luyendyk, K. Matsuoka, J. Mouginot, F. O. Nitsche, Y. Nogi, O. A. Nost, S. V. Popov, E. Rignot, D. M. Rippin, A. Rivera, J. Roberts, N. Ross, M. J. Siegert, A. M. Smith, D. Steinhage, M. Studinger, B. Sun, B. K. Tinto, B. C. Welch, D. Wilson, D. A. Young, C. Xiangbin, and A. Zirizzotti. Bedmap2: improved ice bed, surface and thickness datasets for Antarctica. *The Cryosphere*, 7 (1):375–393, 2013. ISSN 19940416. doi: 10.5194/tc-7-375-2013.

[5] E. Rignot, J. Mouginot, B. Scheuchl, M. Van Den Broeke, M. J. Van Wessem, and M. Morlighem. Four decades of Antarctic ice sheet mass balance from 1979–2017, jan 2019. ISSN 10916490.

[6] E. Larour, H. Seroussi, M. Morlighem, and E. Rignot. Continental scale, high order, high spatial resolution, ice sheet modeling using the Ice Sheet System Model (ISSM). *Journal of Geophysical Research: Earth Surface*, 117 (F1), mar 2012. ISSN 21699011. doi: 10.1029/2011JF002140.

[7] M. Llubes, C. Lanseau, and F. Rémy. Relations between basal condition, subglacial hydrological networks and geothermal flux in Antarctica. *Earth and Planetary Science Letters*, 241(3-4):655–662, jan 2006. ISSN 0012821X. doi: 10.1016/j.epsl.2005.10.040.

[8] C. Van der Veen. *Fundamentals of glacier dynamics*. CRC press, 2013. ISBN 9781439835678.

[9] K. M. Cuffey and W. S. B. Paterson. *The physics of glaciers*. Academic Press, 2010.

[10] A. J. Payne. Limit cycles in the basal thermal regime of ice sheets. *Journal of Geophysical Research: Solid Earth*, 100(B3):4249–4263, 1995.

[11] B. Saltzman. *Dynamical paleoclimatology: generalized theory of global climate change*, volume 80. Elsevier, 2001.

[12] T. M. Jordan, C. N. Williams, D. M. Schroeder, Y. M. Martos, M. A. Cooper, M. J. Siegert, J. D. Paden, P. Huybrechts, and J. L. Bamber. A constraint upon the basal water distribution and thermal state of the Greenland Ice Sheet from radar bed echoes. *Cryosphere*, 12(9):2831–2854, sep 2018. ISSN 19940424. doi: 10.5194/tc-12-2831-2018.

[13] D. J. Brinkerhoff, T. W. Meierbachtol, J. V. Johnson, and J. T. Harper. Sensitivity of the frozen/melted basal boundary to perturbations of basal traction and geothermal heat flux: Isunnguata Sermia, Western Greenland. *Annals of Glaciology*, 52(59):43–50, 2011. doi: 10.3189/172756411799096330.

[14] G. H. Gudmundsson and M. Raymond. On the limit to resolution and information on basal properties obtainable from surface data on ice streams. *The Cryosphere Discussions*, 2(3):413–445, 2008.

[15] D. Maxwell, M. Truffer, S. Avdonin, and M. Stuefer. An iterative scheme for determining glacier velocities and stresses. *Journal of Glaciology*, 54(188): 888–898, 2008.

[16] I. Rogozhina, J. M. Hagedoorn, Z. Martinec, K. Fleming, O. Soucek, R. Greve, and M. Thomas. Effects of uncertainties in the geothermal heat flux distribution on the Greenland Ice Sheet: An assessment of existing heat flow models. *Journal of Geophysical Research: Earth Surface*, 117(F2):n/a–n/a, jun 2012. ISSN 01480227. doi: 10.1029/2011JF002098.

[17] M. Fahnestock, W. Abdalati, I. Joughin, J. Brozena, and P. Gogineni. High geothermal heat flow, basal melt, and the origin of rapid ice flow in central Greenland. *Science*, 294(5550):2338–2342, dec 2001. ISSN 00368075. doi: 10.1126/science.1065370.

[18] C. F. Maule, M. E. Purucker, N. Olsen, and K. Mosegaard. Heat flux anomalies in Antarctica revealed by satellite magnetic data. *Science*, 309(5733): 464–467, jul 2005. ISSN 0036-8075. doi: 10.1126/science.1106888.

[19] C. J. van der Veen, T. Leftwich, R. von Frese, B. M. Csatho, and J. Li. Subglacial topography and geothermal heat flux: Potential interactions with drainage of the Greenland ice sheet. *Geophysical research letters*, 34(12), 2007.

[20] R. E. Bell. The role of subglacial water in ice-sheet mass balance. *Nature Geoscience*, 1(5):297, may 2008. ISSN 17520894. doi: 10.1038/ngeo186.

[21] B. E. Smith, H. A. Fricker, I. R. Joughin, and S. Tulaczyk. An inventory of active subglacial lakes in Antarctica detected by ICESat (2003–2008). *Journal of Glaciology*, 55(192):573–595, 2009.

[22] T. Hondoh, H. Shoji, O. Watanabe, A. N. Salamatin, and V. Y. Lipenkov. Depth-age and temperature prediction at Dome Fuji station, East Antarctica. *Annals of Glaciology*, 35:384–390, 2002. ISSN 02603055. doi: 10.3189/172756402781817013.

[23] D. Dahl-Jensen, V. I. Morgan, and A. Elcheikh. Monte Carlo inverse modelling of the Law Dome (Antarctica) temperature profile. *Annals of Glaciology*, 29(1):145–150, 1999. doi: 10.3189/172756499781821102.

[24] A. N. Salamatin, V. Y. Lipenkov, N. I. Barkov, J. Jouzel, J. R. Petit, and D. Raynaud. Ice core age dating and paleothermometer calibration based on isotope and temperature profiles from deep boreholes at Vostok Station (East Antarctica). *Journal of Geophysical Research*, 103(D8):8963, 1998. ISSN 0148-0227. doi: 10.1029/97JD02253.

[25] C. Ritz, L. Lliboutry, and C. Rado. Analysis of a 870 m deep temperature profile at Dome C. *Annals of Glaciology*, 3:284–289, 1982.

[26] J. A. MacGregor, J. Li, J. D. Paden, G. A. Catania, G. D. Clow, M. A. Fahnestock, S. P. Gogineni, R. E. Grimm, M. Morlighem, S. Nandi, H. Seroussi, and D. E. Stillman. Radar attenuation and temperature within the Greenland Ice Sheet. *Journal of Geophysical Research: Earth Surface*, 120(6):983–1008, jun 2015. ISSN 21699003. doi: 10.1002/2014JF003418.

[27] S. Anandakrishnan, D. D. Blankenship, R. B. Alley, and P. L. Stoffa. Influence of subglacial geology on the position of a West Antarctic ice stream from seismic observations. *Nature*, 394(6688):62, 1998.

[28] D. D. Blankenship, R. E. Bell, S. M. Hodge, J. M. Brozena, J. C. Behrendt, and C. A. Finn. Active volcanism beneath the West Antarctic ice sheet and implications for ice-sheet stability. *Nature*, 361(6412):526, 1993. ISSN 00280836. doi: 10.1038/361526a0.

[29] M. Studinger, R. E. Bell, and A. A. Tikku. Estimating the depth and shape of subglacial Lake Vostok's water cavity from aerogravity data. *Geophysical Research Letters*, 31(12), 2004.

[30] H. A. Fricker, T. Scambos, R. Bindschadler, and L. Padman. An active subglacial water system in West Antarctica mapped from space. *Science*, 315(5818):1544–1548, 2007.

[31] P. Gudmandsen. Electromagnetic probing of ice. In *Electromagnetic probing in geophysics*, volume 79, page 321, 1971.

[32] M. E. Peters, D. D. Blankenship, and D. L. Morse. Analysis techniques for coherent airborne radar sounding: Application to West Antarctic ice streams. *Journal of Geophysical Research: Solid Earth*, 110(B6):1–17, jun 2005. ISSN 21699356. doi: 10.1029/2004JB003222.

[33] J. A. MacGregor, D. P. Winebrenner, H. Conway, K. Matsuoka, P. A. Mayewski, and G. D. Clow. Modeling englacial radar attenuation at Siple

Dome , West Antarctica , using ice chemistry and temperature data. *Journal of Geophysical Research: Earth Surface*, 112(F3):1–14, sep 2007. ISSN 21699011. doi: 10.1029/2006JF000717.

[34] J. A. MacGregor, K. Matsuoka, E. D. Waddington, D. P. Winebrenner, and F. Pattyn. Spatial variation of englacial radar attenuation: Modeling approach and application to the Vostok flowline. *Journal of Geophysical Research: Earth Surface*, 117(F3):1–15, sep 2012. ISSN 21699011. doi: 10.1029/2011JF002327.

[35] D. M. Schroeder, D. D. Blankenship, R. K. Raney, and C. Grima. Estimating subglacial water geometry using radar bed echo specularity: application to Thwaites Glacier, West Antarctica. *IEEE Geoscience and Remote Sensing Letters*, 12(3):443–447, mar 2015. ISSN 1545598X. doi: 10.1109/LGRS.2014.2337878.

[36] V. V. Bogorodsky, C. R. Bentley, and P. E. Gudmandsen. *Radioglaciology*, volume 1. Springer Science & Business Media, 2012.

[37] L. E. Peters, S. Anandakrishnan, R. B. Alley, and D. E. Voigt. Seismic attenuation in glacial ice: A proxy for englacial temperature. *Journal of Geophysical Research: Earth Surface*, 117(2):1–10, jun 2012. ISSN 21699011. doi: 10.1029/2011JF002201.

[38] D. M. Schroeder, C. Grima, and D. D. Blankenship. Evidence for variable grounding-zone and shear-margin basal conditions across Thwaites Glacier, West AntarcticaThwaites grounding zone and shear margin. *Geophysics*, 81 (1):WA35—-WA43, jan 2016. ISSN 19422156. doi: 10.1190/GEO2015-0122.1.

[39] D. M. Schroeder, H. Seroussi, W. Chu, and D. A. Young. Adaptively constraining radar attenuation and temperature across the Thwaites Glacier

catchment using bed echoes. *Journal of Glaciology*, 62(236):1075–1082, dec 2016. ISSN 00221430. doi: 10.1017/jog.2016.100.

[40] M. N. Toksöz, D. H. Johnston, and A. Timur. Attenuation of seismic waves in dry and saturated rocks: I. Laboratory measurements. *GEOPHYSICS*, 44(4):681–690, apr 1979. ISSN 0016-8033. doi: 10.1190/1.1440969.

[41] N. Toksoz. Seismic wave attenuation. *Laboratory measurements*, pages 105–114, 1981.

[42] D. E. Stillman, J. A. MacGregor, and R. E. Grimm. The role of acids in electrical conduction through ice. *Journal of Geophysical Research: Earth Surface*, 118(1):1–16, 2013.

[43] D. M. Schroeder, R. G. Bingham, D. D. Blankenship, K. Christianson, O. Eisen, G. E. Flowers, N. B. Karlsson, M. R. Koutnik, J. D. Paden, and M. J. Siegert. Five decades of radioglaciology. *Annals of Glaciology*, pages 1–13, 2020. doi: 10.1017/aog.2020.11.

[44] M. Morlighem, C. N. Williams, E. Rignot, L. An, J. E. Arndt, J. L. Bamber, G. Catania, N. Chauché, J. A. Dowdeswell, B. Dorschel, I. Fenty, K. Hogan, I. Howat, A. Hubbard, M. Jakobsson, T. M. Jordan, K. K. Kjeldsen, R. Millan, L. Mayer, J. Mouginot, B. P. Noël, C. O'Cofaigh, S. Palmer, S. Rysgaard, H. Seroussi, M. J. Siegert, P. Slabon, F. Straneo, M. R. van den Broeke, W. Weinrebe, M. Wood, and K. B. Zinglersen. BedMachine v3: Complete Bed Topography and Ocean Bathymetry Mapping of Greenland From Multibeam Echo Sounding Combined With Mass Conservation. *Geophysical Research Letters*, 44(21):11,051–11,061, nov 2017. ISSN 19448007. doi: 10.1002/2017GL074954.

[45] S. Gogineni, D. Tammana, D. Braaten, C. Leuschen, T. Akins, J. Legarsky, P. Kanagaratnam, J. Stiles, C. Allen, and K. Jezek. Coherent radar ice

thickness measurements over the Greenland ice sheet. *Journal of Geophysical Research Atmospheres*, 106(D24):33761–33772, dec 2001. ISSN 01480227. doi: 10.1029/2001JD900183.

[46] H. F. Corr, A. Jenkins, K. W. Nicholls, and C. S. Doake. Precise measurement of changes in ice-shelf thickness by phase-sensitive radar to determine basal melt rates. *Geophysical Research Letters*, 29(8):73, apr 2002. ISSN 19448007. doi: 10.1029/2001GL014618.

[47] C. Martín, G. H. Gudmundsson, H. D. Pritchard, and O. Gagliardini. On the effects of anisotropic rheology on ice flow, internal structure, and the age-depth relationship at ice divides. *Journal of Geophysical Research*, 114 (F4):F04001, oct 2009. ISSN 0148-0227. doi: 10.1029/2008JF001204.

[48] K. Matsuoka, D. Morse, and C. F. Raymond. Estimating englacial radar attenuation using depth profiles of the returned power, central West Antarctica. *Journal of Geophysical Research: Earth Surface*, 115(F2):1–15, jun 2010. doi: 10.1029/2009JF001496.

[49] F. NG and E. C. King. Kinematic waves in polar firn stratigraphy. *Journal of Glaciology*, 57(206):1119–1134, sep 2011. ISSN 0022-1430. doi: 10.3189/002214311798843340.

[50] J. T. Bailey, S. Evans, and G. D. Q. Robin. Radio echo sounding of polar ice sheets. *Nature*, 204(4957):420–421, 1964. ISSN 00280836. doi: 10.1038/204420a0.

[51] P. Gudmandsen. Airborne Radio Echo Sounding of the Greenland Ice Sheet. *The Geographical Journal*, 135(4):548, dec 1969. ISSN 00167398. doi: 10.2307/1795099.

[52] J. L. Bamber, J. A. Griggs, R. T. Hurkmans, J. A. Dowdeswell, S. P. Gogineni, I. Howat, J. Mouginot, J. Paden, S. Palmer, E. Rignot, and D. Steinhage. A new bed elevation dataset for Greenland. *Cryosphere*, 7(2):499–510, 2013. ISSN 19940416. doi: 10.5194/tc-7-499-2013.

[53] G. K. Oswald and S. P. Gogineni. Recovery of subglacial water extent from Greenland radar survey data. *Journal of Glaciology*, 54(184):94–106, 2008. ISSN 00221430. doi: 10.3189/002214308784409107.

[54] D. M. Schroeder, D. D. Blankenship, and D. A. Young. Evidence for a water system transition beneath Thwaites Glacier, West Antarctica. *Proceedings of the National Academy of Sciences*, 110(30):12225–12228, jul 2013. ISSN 0027-8424. doi: 10.1073/pnas.1302828110.

[55] C. Grima, D. M. Schroeder, D. D. Blankenship, and D. A. Young. Planetary landing-zone reconnaissance using ice-penetrating radar data: Concept validation in Antarctica. *Planetary and Space Science*, 103:191–204, nov 2014. ISSN 00320633. doi: 10.1016/j.pss.2014.07.018.

[56] M. S. Haynes, E. Chapin, and D. M. Schroeder. Geometric Power Fall-Off in Radar Sounding. *IEEE Transactions on Geoscience and Remote Sensing*, 56(11):6571–6585, nov 2018. ISSN 0196-2892. doi: 10.1109/TGRS.2018.2840511.

[57] M. S. Haynes. Surface and subsurface radar equations for radar sounders. *Annals of Glaciology*, pages 1–8, apr 2020. ISSN 0260-3055. doi: 10.1017/aog.2020.16.

[58] C. L. Stewart, P. Christoffersen, K. W. Nicholls, M. J. M. Williams, and J. A. Dowdeswell. Basal melting of Ross Ice Shelf from solar heat absorption in an ice-front polynya. *Nature Geoscience*, 12(6):435–440, jun 2019. ISSN 1752-0894. doi: 10.1038/s41561-019-0356-0.

[59] D. W. Ashmore and R. G. Bingham. Antarctic subglacial hydrology: Current knowledge and future challenges. *Antarctic Science*, 26(6):758–773, nov 2014. ISSN 13652079. doi: 10.1017/S0954102014000546.

[60] W. Chu, D. M. Schroeder, H. Seroussi, T. T. Creyts, and R. E. Bell. Complex Basal Thermal Transition Near the Onset of Petermann Glacier, Greenland. *Journal of Geophysical Research: Earth Surface*, 123(5):985–995, may 2018. ISSN 21699011. doi: 10.1029/2017JF004561.

[61] S. Nerozzi and J. W. Holt. Earliest accumulation history of the north polar layered deposits, Mars from SHARAD. *Icarus*, 308:128–137, jul 2018. ISSN 00191035. doi: 10.1016/j.icarus.2017.05.027.

[62] B. H. Hills, K. Christianson1, N. Holschuh1, B. H. Hills, K. Christianson, N. Holschuh, B. H. Hills, K. Christianson, N. Holschuh, and N. Holschuh. A framework for attenuation method selection evaluated with ice-penetrating radar data at South Pole Lake. *Annals of Glaciology*, pages 1–12, may 2020. ISSN 0260-3055. doi: 10.1017/aog.2020.32.

[63] K. Matsuoka, J. A. Macgregor, and F. Pattyn. Pitfalls in radar diagnosis of ice-sheet bed conditions: Lessons from englacial attenuation models. *Geophysical Research Letters*, 38(5):1–5, mar 2011. ISSN 00948276. doi: 10.1029/2010GL046205.

[64] Robert W Jacobel, Brian C Welch, David Osterhouse, Rickard Pettersson, and Joseph A Macgregor. Spatial variation of radar-derived basal conditions on Kamb Ice Stream, West Antarctica. *Annals of Glaciology*, 50(51):10–16, 2009. ISSN 02603055. doi: 10.3189/172756409789097504.

[65] T. M. Jordan, J. L. Bamber, C. N. Williams, J. D. Paden, M. J. Siegert, P. Huybrechts, O. Gagliardini, and F. Gillet-Chaulet. An ice-sheet-wide framework for englacial attenuation from ice-penetrating radar data. *Cryosphere*, 10(4):1547–1570, jul 2016. ISSN 19940424. doi: 10.5194/tc-10-1547-2016.

[66] K. Matsuoka, J. A. MacGregor, and F. Pattyn. Predicting radar attenuation within the Antarctic ice sheet. *Earth and Planetary Science Letters*, 359: 173–183, dec 2012. ISSN 0012821X. doi: 10.1016/j.epsl.2012.10.018.

[67] K. Christianson, R. W. Jacobel, H. J. Horgan, R. B. Alley, S. Anandakrishnan, D. M. Holland, and K. J. DallaSanta. Basal conditions at the grounding zone of Whillans Ice Stream, West Antarctica, from ice-penetrating radar. *Journal of Geophysical Research: Earth Surface*, 121(11):1954–1983, nov 2016. ISSN 21699011. doi: 10.1002/2015JF003806.

[68] J. A. Macgregor, G. A. Catania, H. Conway, D. M. Schroeder, I. Joughin, D. A. Young, S. D. Kempf, and D. D. Blankenship. Weak bed control of the eastern shear margin of Thwaites Glacier, West Antarctica. *Journal of Glaciology*, 59(217):900–912, oct 2013. ISSN 00221430. doi: 10.3189/2013JoG13J050.

[69] F. A. M. Falcini, D. M. Rippin, M. Krabbendam, and K. A. Selby. Quantifying bed roughness beneath contemporary and palaeo-ice streams. 2020. doi: 10.1017/jog.2018.71.

[70] J. Weertman. On the Sliding of Glaciers. *Journal of Glaciology*, 3(21):33–38, 1957. ISSN 0022-1430. doi: 10.1017/s0022143000024709.

[71] C. Schoof. Basal perturbations under ice streams: Form drag and surface expression. *Journal of Glaciology*, 48(162):407–416, 2002. ISSN 00221430. doi: 10.3189/172756502781831269.

[72] W. Chu, D. M. Schroeder, and M. R. Siegfried. Retrieval of Englacial Firn Aquifer Thickness From Ice-Penetrating Radar Sounding in Southeastern Greenland. *Geophysical Research Letters*, 45(21):11,770–11,778, nov 2018. ISSN 19448007. doi: 10.1029/2018GL079751.

[73] J. W. Glen and J. G. Paren. The Electrical Properties of Snow and Ice. *Journal of Glaciology*, 15(73):15–38, jan 1975. ISSN 0022-1430. doi: 10.3189/S0022143000034249.

[74] G. P. Johari and P. A. Charette. The Permittivity and Attenuation in Polycrystalline and Single-Crystal Ice Ih at 35 and 60 MHz. *Journal of Glaciology*, 14(71):293–303, 1975. ISSN 0022-1430. doi: 10.3189/s002214300002178x.

[75] J. C. Moore and S. Fujita. Dielectric properties of ice containing acid and salt impurity at microwave and low frequencies. *Journal of Geophysical Research*, 98(B6):9769, 1993. ISSN 0148-0227. doi: 10.1029/93JB00710.

[76] E. Pettinelli, B. Cosciotti, F. Di Paolo, S. E. Lauro, E. Mattei, R. Orosei, and G. Vannaroni. Dielectric properties of Jovian satellite ice analogs for subsurface radar exploration: A review. *Reviews of Geophysics*, 53(3):593–641, sep 2015. ISSN 87551209. doi: 10.1002/2014RG000463.

[77] M. J. Wolovick, R. E. Bell, T. T. Creyts, and N. Frearson. Identification and control of subglacial water networks under Dome A, Antarctica. *Journal of Geophysical Research: Earth Surface*, 118(1):140–154, mar 2013. ISSN 21699003. doi: 10.1029/2012JF002555.

[78] S. Shabtaie, I. M. Whillans, and C. R. Bentley. The morphology of ice streams A, B, and C, West Antarctica, and their environs. *Journal of Geophysical Research*, 92(B9):8865–8883, 1987. ISSN 01480227. doi: 10.1029/JB092iB09p08865.

[79] D. Winebrenner, B. Smith, G. Catania, H. Conway, and C. Raymond. Radio frequency attenuation beneath Siple Dome, West Antarctica, from wide angle and profiling radar observations. *Annals of Glaciology*, 37:1–7, 2003.

[80] N. Holschuh, K. Christianson, S. Anandakrishnan, R. B. Alley, and R. W. Jacobel. Constraining attenuation uncertainty in common midpoint radar surveys of ice sheets. *Journal of Geophysical Research: Earth Surface*, 121 (10):1876–1890, oct 2016. ISSN 21699011. doi: 10.1002/2016JF003942.

[81] J. A. Macgregor, S. Anandakrishnan, G. A. Catania, and D. P. Winebrenner. The grounding zone of the Ross Ice Shelf, West Antarctica, from ice-penetrating radar. *Journal of Glaciology*, 57(205):917–928, oct 2011. ISSN 00221430. doi: 10.3189/002214311798043780.

[82] D. J. Walker. *Glaciological and geophysical studies in Wilkes Land, Antarctica, 1962/63*. PhD thesis, University of Melbourne, Department of Meteorology, 1976.

[83] D. D. Blankenship, S. D. Kempf, and D. Young. IceBridge HiCARS 1 L2 Geolocated Ice Thickness Version 1.0. *NASA Distributed Active Archive Center (DAAC) at the National Snow and Ice Data Center (NSIDC)*, 2011.

[84] D. A. Young, A. P. Wright, J. L. Roberts, R. C. Warner, N. W. Young, J. S. Greenbaum, D. M. Schroeder, J. W. Holt, D. E. Sugden, D. D. Blankenship, and Others. A dynamic early East Antarctic Ice Sheet suggested by ice-covered fjord landscapes. *Nature*, 474(7349):72, 2011.

[85] J. Roberts, C. Plummer, T. Vance, T. van Ommen, A. Moy, S. Poynter, A. Treverrow, M. Curran, and S. George. A 2000-year annual record of snow accumulation rates for Law Dome, East Antarctica. *Climate of the Past*, 11 (5):697–707, may 2015. ISSN 1814-9332. doi: 10.5194/cp-11-697-2015.

[86] D. M. Etheridge, L. P. Steele, R. L. Langenfelds, R. J. Francey, J.-M. Barnola, and V. I. Morgan. Historical CO2 records from the Law Dome DE08, DE08-2, and DSS ice cores. *Trends: a compendium of data on global change*, pages 351–364, 1998.

[87] V. I. Morgan, C. W. Wookey, J. Li, T. D. Van Ommen, W. Skinner, and M. Fitzpatrick. Site information and initial results from deep ice drilling on Law Dome, Antarctica. *Journal of Glaciology*, 43(143):3–10, 1997. ISSN 0022-1430. doi: 10.3189/s0022143000002768.

[88] T. Haran, J. Bohlander, T. Scambos, T. Painter, and M. Fahnestock. MODIS Mosaic of Antarctica 2008-2009 (MOA2009). *National Snow and Ice Data Center*, 2014. doi: 10.7265/N5KP8037.

[89] T. A. Scambos, T. M. Haran, M. A. Fahnestock, T. H. Painter, and J. Bohlander. MODIS-based Mosaic of Antarctica (MOA) data sets: Continent-wide surface morphology and snow grain size. *Remote Sensing of Environment*, 111(2):242–257, nov 2007. ISSN 00344257. doi: 10.1016/j.rse.2006.12.020.

[90] C. A. Greene, D. E. Gwyther, and D. D. Blankenship. Antarctic Mapping Tools for MATLAB. *Computers and Geosciences*, 104:151–157, jul 2017. ISSN 00983004. doi: 10.1016/j.cageo.2016.08.003.

[91] H. Engelhardt. Thermal regime and dynamics of the West Antarctic ice sheet. *Annals of Glaciology*, 39:85–92, 2004.

[92] K. W. Nicholls, J. G. Paren, K. W. Nicholls, and J. G. Paren. Extending the Antarctic Meteorological Record Using Ice-Sheet Temperature Profiles. *Journal of Climate*, 6(1):141–150, jan 1993. doi: 10.1175/1520-0442(1993)006⟨0141:ETAMRU⟩2.0.CO;2.

[93] V. Zagorodnov, O. Nagornov, T. A. Scambos, A. Muto, E. Mosley-Thompson, E. C. Pettit, and S. Tyuflin. Borehole temperatures reveal details of 20th century warming at Bruce Plateau, Antarctic Peninsula. *The Cryosphere*, 6(3):675–686, 2012. doi: 10.5194/tc-6-675-2012.

[94] D. J. Easterbrook. *Surface processes and landforms*. Pearson College Division, 1999.

[95] R. Greve and H. Blatter. *Dynamics of ice sheets and glaciers*. Springer Science & Business Media, 2009.

[96] R. G. Bingham and M. J. Siegert. Radio-Echo Sounding Over Polar Ice Masses. *Journal of Environmental & Engineering Geophysics*, 12(1):47–62, mar 2007. ISSN 1083-1363. doi: 10.2113/JEEG12.1.47.

[97] J. M. Reynolds. *An introduction to applied and environmental geophysics*. John Wiley & Sons, 2011.

[98] K. Matsuoka, J. A. MacGregor, and F. Pattyn. Using englacial radar attenuation to better diagnose the subglacial environment: A review. In *Proceedings of the 13th Internarional Conference on Ground Penetrating Radar*, pages 1–5. IEEE, 2010. ISBN 9781424446049. doi: 10.1109/ICGPR.2010.5550161.

[99] C. R. Bentley, N. Lord, G. Liu, and C. Liu. Radar reflections reveal a wet bed beneath stagnant Ice Stream C and a frozen bed beneath ridge BC, West Antarctica. *Journal of Glaciology*, 44(146):149–156, jan 1998. ISSN 0022-1430. doi: 10.1017/S0022143000002434.

[100] D. M. Rippin, J. L. Bamber, M. J. Siegert, D. G. Vaughan, and H. F. Corr. The role of ice thickness and bed properties on the dynamics of the enhanced-flow tributaries of Bailey Ice Stream and Slessor Glacier, East

Antarctica. *Annals of Glaciology*, 39:366–372, 2004. ISSN 02603055. doi: 10.3189/172756404781814375.

[101] R. W. Jacobel, K. E. Lapo, J. R. Stamp, B. W. Youngblood, B. C. Welch, and J. L. Bamber. A comparison of basal reflectivity and ice velocity in East Antarctica. *Cryosphere*, 4(4):447–452, 2010. ISSN 19940416. doi: 10.5194/tc-4-447-2010.

[102] G. D. Q. d. Q. Robin, S. Evans, and J. T. Bailey. Interpretation of radio echo sounding in polar ice sheets. *Phil. Trans. R. Soc. Lond. A*, 265(1166): 437–505, dec 1969. ISSN 1364-503X. doi: 10.1098/rsta.1969.0063.

[103] T. Barrella, S. Barwick, and D. Saltzberg. Ross Ice Shelf (Antarctica) in situ radio-frequency attenuation. *Journal of Glaciology*, 57(201):61–66, 2011.

[104] A. P. Wright, D. A. Young, J. L. Roberts, D. M. Schroeder, J. L. Bamber, J. A. Dowdeswell, N. W. Young, A. M. Le Brocq, R. C. Warner, A. J. Payne, D. D. Blankenship, T. D. Van Ommen, M. J. Siegert, and Others. Evidence of a hydrological connection between the ice divide and ice sheet margin in the Aurora Subglacial Basin, East Antarctica. *Journal of Geophysical Research: Earth Surface*, 117(1):1–15, 2012. ISSN 21699011. doi: 10.1029/2011JF002066.

[105] IceBridge HiCARS 2 L0 Raw Return Energy Amplitudes, Version 1 — National Snow and Ice Data Center, 2011.

[106] A. Zirizzotti, L. Cafarella, S. Urbini, and J. A. Baskaradas. Electromagnetic ice absorption rate at Dome C, Antarctica. *Journal of Glaciology*, 60(223): 849–854, 2014. ISSN 00221430. doi: 10.3189/2014JoG13J208.

[107] A. Zirizzotti, L. Cafarella, S. Urbini, J. A. Baskaradas, and A. Settimi. Assessment of Electromagnetic Absorption of Ice from Ice Core Measurements.

IEEE Transactions on Geoscience and Remote Sensing, 54(8):4758–4763, 2016. ISSN 01962892. doi: 10.1109/TGRS.2016.2551300.

[108] J. A. MacGregor, K. Matsuoka, and M. Studinger. Radar detection of accreted ice over Lake Vostok, Antarctica. *Earth and Planetary Science Letters*, 282(1-4):222–233, may 2009. ISSN 0012821X. doi: 10.1016/j.epsl.2009.03.018.

[109] D. I. Warton. Penalized normal likelihood and ridge regularization of correlation and covariance matrices. *Journal of the American Statistical Association*, 103(481):340–349, 2008.

[110] A. E. Hoerl and R. W. Kennard. Ridge regression: Biased estimation for nonorthogonal problems. *Technometrics*, 12(1):55–67, 1970.

[111] R. Tibshirani. Regression shrinkage and selection via the lasso. *Journal of the Royal Statistical Society: Series B (Methodological)*, 58(1):267–288, 1996.

[112] T. Thorsteinsson. An analytical approach to deformation of anisotropic ice-crystal aggregates. *Journal of Glaciology*, 47(158):507–516, sep 2001. ISSN 0022-1430. doi: 10.3189/172756501781832124.

[113] E. Larour, M. Morlighem, H. Seroussi, J. Schiermeier, and E. Rignot. Ice flow sensitivity to geothermal heat flux of Pine Island Glacier, Antarctica. *Journal of Geophysical Research F: Earth Surface*, 117(4):1–12, dec 2012. ISSN 01480227. doi: 10.1029/2012JF002371.

[114] D. P. Hasterok. *Thermal state of continental and oceanic lithosphere*. PhD thesis, The University of Utah, 2010.

[115] A. T. Fisher, K. D. Mankoff, S. M. Tulaczyk, S. W. Tyler, N. Foley, and Others. High geothermal heat flux measured below the West Antarctic Ice

Sheet. *Science advances*, 1(6):e1500093, jul 2015. ISSN 23752548. doi: 10.1126/sciadv.1500093.

[116] A. Burton-Johnson, R. Dziadek, and C. Martin. Geothermal heat flow in Antarctica: current and future directions. *The Cryosphere Discussions*, (March):1–45, 2020. ISSN 1994-0416. doi: 10.5194/tc-2020-59.

[117] N. M. Shapiro and M. H. Ritzwoller. Inferring surface heat flux distributions guided by a global seismic model: particular application to Antarctica. *Earth and Planetary Science Letters*, 223(1):213–224, jun 2004. ISSN 0012-821X. doi: https://doi.org/10.1016/j.epsl.2004.04.011.

[118] Y. M. Martos, M. Catalán, T. A. Jordan, A. Golynsky, D. Golynsky, G. Eagles, and D. G. Vaughan. Heat flux distribution of Antarctica unveiled. *Geophysical Research Letters*, 44(22):11–417, nov 2017. ISSN 19448007. doi: 10.1002/2017GL075609.

[119] H. N. Pollack, S. J. Hurter, and J. R. Johnson. Heat flow from the Earth's interior: Analysis of the global data set, aug 1993. ISSN 19449208.

[120] G. R. Beardsmore and J. P. Cull. *Crustal heat flow: a guide to measurement and modelling*. Cambridge University Press, aug 2001. doi: 10.1017/cbo9780511606021.

[121] W. Lowrie. *Fundamentals of Geophysics*. Cambridge University Press, 2007. doi: 10.1017/cbo9780511807107.

[122] W. F. McDonough and S. s. Sun. The composition of the Earth. *Chemical Geology*, 120(3-4):223–253, mar 1995. ISSN 00092541. doi: 10.1016/0009-2541(94)00140-4.

[123] D. R. Boden. Geology and Heat Architecture of the Earth's Interior. *Geologic Fundamentals of Geothermal Energy*, pages 53–70, oct 2016. doi: 10.1201/9781315371436-4.

[124] C. B. Begeman, S. M. Tulaczyk, and A. T. Fisher. Spatially Variable Geothermal Heat Flux in West Antarctica: Evidence and Implications. *Geophysical Research Letters*, 44(19):9823–9832, oct 2017. ISSN 19448007. doi: 10.1002/2017GL075579.

[125] T. Hughes. Modeling ice sheets from the bottom up. *Quaternary Science Reviews*, 28:1831–1849, 2009. doi: 10.1016/j.quascirev.2009.06.004.

[126] H. Goelzer, A. Robinson, H. Seroussi, and R. S. van de Wal. Recent Progress in Greenland Ice Sheet Modelling. *Current Climate Change Reports*, 3(4): 291–302, 2017. ISSN 21986061. doi: 10.1007/s40641-017-0073-y.

[127] G. J. Leysinger Vieli, C. Martín, R. C. Hindmarsh, and M. P. Lüthi. Basal freeze-on generates complex ice-sheet stratigraphy. *Nature Communications*, 9(1), dec 2018. ISSN 20411723. doi: 10.1038/s41467-018-07083-3.

[128] M. An, D. A. Wiens, Y. Zhao, M. Feng, A. Nyblade, M. Kanao, Y. Li, A. Maggi, and J. J. Lévêque. Temperature, lithosphere-asthenosphere boundary, and heat flux beneath the Antarctic Plate inferred from seismic velocities. *Journal of Geophysical Research: Solid Earth*, 120(12):8720–8742, dec 2015. ISSN 21699356. doi: 10.1002/2015JB011917.

[129] A. Pollett, D. Hasterok, T. Raimondo, J. A. Halpin, M. Hand, B. Bendall, S. McLaren, J. A. Halpin, M. Hand, B. Bendall, and S. McLaren. Heat Flow in Southern Australia and Connections With East Antarctica Geochemistry , Geophysics , Geosystems. *Geochemistry, Geophysics, Geosystems*, 20(11): 5352–5370, nov 2019. ISSN 15252027. doi: 10.1029/2019GC008418.

[130] M. Lösing, J. Ebbing, and W. Szwillus. No Title, apr 2020. ISSN 2296-6463.

[131] H. Engelhardt. Ice temperature and high geothermal flux at Siple Dome, West Antarctica, from borehole measurements. *Journal of Glaciology*, 50 (169):251–256, 2004. ISSN 00221430. doi: 10.3189/172756504781830105.

[132] T. J. Fudge, S. C. Biyani, D. Clemens-Sewall, and R. L. Hawley. Constraining Geothermal Flux at Coastal Domes of the Ross Ice Sheet, Antarctica. *Geophysical Research Letters*, 46(22):13090–13098, nov 2019. ISSN 0094-8276. doi: 10.1029/2019GL084332.

[133] M. Purucker. Geothermal heat flux data set based on low resolution observations collected by the CHAMP satellite between 2000 and 2010, and produced from the MF-6 model following the technique described in Fox Maule et al.(2005). *See http://websrv. cs. umt. edu/isis/index. php*, 2013.

[134] F. Pappa, J. Ebbing, and F. Ferraccioli. Moho Depths of Antarctica: Comparison of Seismic, Gravity, and Isostatic Results. *Geochemistry, Geophysics, Geosystems*, 20(3):1629–1645, mar 2019. ISSN 15252027. doi: 10.1029/2018GC008111.

[135] F. Pappa, J. Ebbing, F. Ferraccioli, and W. van der Wal. Modeling Satellite Gravity Gradient Data to Derive Density, Temperature, and Viscosity Structure of the Antarctic Lithosphere. *Journal of Geophysical Research: Solid Earth*, 124(11):12053–12076, nov 2019. ISSN 21699356. doi: 10.1029/2019JB017997.

[136] T. A. Jordan, C. Martin, F. Ferraccioli, K. Matsuoka, H. Corr, R. Forsberg, A. Olesen, and M. Siegert. Anomalously high geothermal flux near the South Pole. *Scientific reports*, 8(1):16785, nov 2018. ISSN 2045-2322. doi: 10.1038/s41598-018-35182-0.

[137] L. Mony, J. L. Roberts, and J. A. Halpin. Inferring geothermal heat flux from an ice-borehole temperature profile at Law Dome, East Antarctica. *Journal of Glaciology*, 66(257):509–519, jun 2020. ISSN 00221430. doi: 10.1017/jog.2020.27.

[138] C. J. Carson, S. McLaren, J. L. Roberts, S. D. Boger, and D. D. Blankenship. Hot rocks in a cold place: high sub-glacial heat flow in East Antarctica. *Journal of the Geological Society*, 171(1):9–12, 2014. ISSN 0016-7649. doi: 10.1144/jgs2013-030.

[139] P. R. F. Barnes. Effect of density on electrical conductivity of chemically laden polar ice. *Journal of Geophysical Research*, 107(B2), 2002. ISSN 0148-0227. doi: 10.1029/2000jb000080.

[140] Y.-C. Yen. *Review of thermal properties of snow, ice, and sea ice*, volume 81. US Army, Corps of Engineers, Cold Regions Research and Engineering Laboratory, 1981.

[141] J. M. Van Wessem, C. H. Reijmer, M. Morlighem, J. Mouginot, E. Rignot, B. Medley, I. Joughin, B. Wouters, M. A. Depoorter, J. L. Bamber, J. T. Lenaerts, W. J. Van De Berg, M. R. Van Den Broeke, and E. Van Meijgaard. Improved representation of East Antarctic surface mass balance in a regional atmospheric climate model. *Journal of Glaciology*, 60(222):761–770, jul 2014. ISSN 00221430. doi: 10.3189/2014JoG14J051.

[142] J. D'Errico. Surface Fitting using gridfit. *MATLAB Central File Exchange*, 2020.

[143] M. Morlighem, E. Rignot, H. Seroussi, E. Larour, H. Ben Dhia, and D. Aubry. Spatial patterns of basal drag inferred using control methods from a full-Stokes and simpler models for Pine Island Glacier, West Antarctica.

Geophysical Research Letters, 37(14):1–6, 2010. ISSN 00948276. doi: 10.1029/2010GL043853.

[144] J. A. Macgregor, M. A. Fahnestock, G. A. Catania, J. D. Paden, S. P. Gogineni, S. K. Young, S. C. Rybarski, A. N. Mabrey, B. M. Wagman, M. Morlighem, S. Prasad Gogineni, S. K. Young, S. C. Rybarski, A. N. Mabrey, B. M. Wagman, and M. Morlighem. Radiostratigraphy and age structure of the Greenland Ice Sheet. *Journal of Geophysical Research: Earth Surface*, 120(2):212–241, feb 2015. ISSN 21699011. doi: 10.1002/2014JF003215.

[145] R. G. Bingham, D. M. Rippin, N. B. Karlsson, H. F. J. Corr, F. Ferraccioli, T. A. Jordan, A. M. Le Brocq, K. C. Rose, N. Ross, and M. J. Siegert. Ice-flow structure and ice dynamic changes in the Weddell Sea sector of West Antarctica from radar-imaged internal layering. *Journal of Geophysical Research: Earth Surface*, 120(4):655–670, apr 2015. ISSN 2169-9003. doi: 10.1002/2014JF003291.

[146] M. G. Cavitte, D. D. Blankenship, D. A. Young, D. M. Schroeder, F. Parrenin, E. Lemeur, J. A. MacGregor, and M. J. Siegert. Deep radiostratigraphy of the East Antarctic plateau: Connecting the Dome C and Vostok ice core sites. *Journal of Glaciology*, 62(232):323–334, apr 2016. ISSN 00221430. doi: 10.1017/jog.2016.11.

[147] G. K. A. Oswald, S. Rezvanbehbahani, and L. A. Stearns. Radar evidence of ponded subglacial water in Greenland. *Journal of Glaciology*, 64(247): 711–729, oct 2018. ISSN 0022-1430. doi: 10.1017/jog.2018.60.